Synthesis, Crystal Structure, and Physical Properties of the Type-I Clathrate Ba8–δNix ySi46–x–y

Umut Aydemir, Christophe Candolfi, Alim Ormeci, Horst Borrmann, Ulrich Burkhardt, Yigit Oztan, Niels Oeschler, Michael Baitinger, Franck Steglich, Yuri Grin

Synthesis, Crystal Structure and Physical Properties of the Clathrate-I $Ba_{8-\delta}Ni_x\square_ySi_{46-x-y}$

*U. Aydemir, C. Candolfi, A. Ormeci, H. Borrmann, U. Burkhardt, Y. Oztan, N. Oeschler, M. Baitinger, F. Steglich and Yu. Grin**

Max-Planck Institut für Chemische Physik fester Stoffe, Nöthnitzer Straße 40, 01187 Dresden

grin@cpfs.mpg.de

RECEIVED DATE (…)

Type-I clathrate phase $Ba_{8-\delta}Ni_x\square_ySi_{46-x-y}$ has been synthesized for (δ = 0, 0.1; $1.6 \leq x \leq 3.8$; $0 \leq y \leq 0.9$; $\square$ = vacancy) from the elements. The homogeneity range was revealed by microprobe analyses and powder X-ray diffraction (PXRD) data. The phase crystallizes in the space group $Pm\bar{3}n$ (no. 223). Analyses of single-crystal X-ray diffraction data together with microprobe analysis indicate the presence of framework defects for compositions with higher Ni content. Within the homogeneity range, the lattice parameter decreases from a = 10.3088(1) Å for $Ba_{7.9}Ni_{1.6}Si_{44.4}$ to a = 10.2896(1) Å for $Ba_8Ni_{3.8}Si_{41.3}$. Chemical bonding was analyzed based on the electron localizability indicator (ELI). Ni *K*-edge X-ray absorption spectroscopy measurements on investigated compositions indicate oxidation state close to elemental Ni. Low-temperature electrical resistivity measurements revealed superconductivity onsets at 6.0 K and 5.5 K for the compositions $Ba_{7.9}Ni_{1.6}Si_{44.4}$ and $Ba_{7.9}Ni_{1.7}Si_{44.3}$, respectively. Thermoelectric properties including electrical resistivity, thermopower and thermal conductivity were further investigated in the temperature range 300 - 773 K to assess the thermoelectric potential of this phase. Regardless of the Ni content, the samples exhibit metallic-like behavior resulting

in moderate thermopower values. The thermal conductivity values are low ranging from 4 to 7 $Wm^{-1}K^{-1}$ in the investigated temperature range.

KEYWORDS. Clathrate-I, Phase formation, Superconductivity, Vacancy, Chemical bonding

1. INTRODUCTION

Type-I silicon clathrates are known since the crystal structure of Na_8Si_{46} was revealed by Kasper and Hagenmuller in 1965.[1] In the crystal structure, Si atoms form a 4-connected, covalently-bonded framework with 20-atom and 24-atom polyhedral cages filled by Na atoms. The valence electrons of Na are not needed for the formation of the four bonded silicon framework. Na_8Si_{46} shows metallic behavior,[2] which implies that the excess electrons occupy antibonding conduction bands. It was first shown by Yamanaka et al. in 1995 that the Si_{46} framework can be filled by Ba atoms and bear even larger amounts of excess electrons as in $Na_2Ba_6Si_{46}$.[3] This phase attracted considerable attention since it was found to be the first superconductor based on an sp^3-framework with $T_c \approx 4$ K.[4] A higher transition temperature of $T_c \approx 8$ K was found for Ba_8Si_{46}.[5] Ternary superconducting clathrates have been reported, in which silicon atoms are partially replaced with other elements, e.g. Ge,[6] Ga,[7] Cu,[8] Ag.[9] However, in all cases, T_c was found to decrease with content of substitution atoms and superconductivity vanishes after a certain substitution level is reached. For most of the clathrate-I silicides, the number of excess electrons of the cage atoms is reduced by substitution atoms in the framework and when full charge balance is achieved, semiconducting clathrates can be obtained. In the Zintl phase $Ba_8Ga_{16}Si_{30}$, e.g., Si atoms are substituted by Ga resulting in the charge balance $(Ba^{2+})_8(Ga^-)_{16}(Si^0)_{30}$.[10-12] Such phases are of high interest for their thermoelectric properties,[13] which depend on thermopower (α), electrical resistivity (ρ) and thermal conductivity (λ) through dimensionless thermoelectric figure-of-merit, $ZT = (\alpha^2 T)/(\rho\lambda)$. Intermetallic clathrates show favorably low lattice thermal conductivity almost regardless of composition. Hence, clathrates with high thermoelectric efficiency might be achieved by optimizing thermopower and electrical resistivity. In this respect, clathrate systems with a preferably large homogeneity range are promising candidates, which allow for tuning the charge carrier concentration through chemical composition. For example, clathrates of the system Ba–Ni–Ge show either *p*- or *n*-type conduction behavior depending on the Ni content.[14, 15] For the system Ba–Ni–Si, a clathrate-I phase was reported only for the composition $Ba_8Ni_{1.8}Si_{44.2}$.[16] Crystals of this phase could be directly obtained from the melt, which is remarkable, because the binary Ba_8Si_{46} has been prepared

under high pressure conditions. Surprisingly, the reported lattice parameter of $Ba_8Ni_{1.8}Si_{44.2}$ (a = 10.285(5) Å) is significantly smaller than even that of Ba_8Si_{46} (a = 10.328(2) Å). In this regard, more systematic studies were required to determine the phase formation and the variations in the crystal structure with the Ni content.

Recently, we reported a thorough theoretical and experimental investigation of the electronic band structure and the low-temperature transport properties of type-I clathrates in the system Ba – Ni – Si.[17] Herein, we expand our investigations to the phase relations and the homogeneity range of the clathrate I phase $Ba_{8-\delta}Ni_x\square_ySi_{46-x-y}$. We discuss the crystal structure taking into account the presence of vacancies in the framework, which is generally not considered for silicon clathrates. In addition, first-principles electronic structure calculations were carried out to further assess phase stability and chemical bonding. X-ray absorption spectroscopy (XAS) measurements were performed to asses the oxidation state of Ni in the clathrate compounds. We demonstrate the possibility of achieving phase-pure samples with lower Ni contents paving the way for a systematic study of the evolution of superconductivity as a function of Ni content. Finally, thermoelectric potential of the clathrate phase at high temperatures was studied.

2. EXPERIMENTAL SECTION

2.1 Synthesis. Sample preparations were performed in an argon-filled glove box. Polycrystalline samples were synthesized by reaction of crystalline Ba (ChemPur, 99.9% metals basis), Ni powder (Chempur, 99.9% metals basis) and ground Si pieces (ChemPur, 99.9999% metals basis). Stoichiometric amounts of elements with total weights of around 2 g were placed in an open glassy carbon crucible (Ø = 12 mm, l = 12mm, Sigradur G, HTW) and slowly heated to the melt using an induction furnace (5 kW, coil Ø = 40 mm, l = 35 mm, Hüttinger; IR-Pyrometer, Maurer). As solidified products were difficult to remove from the crucible, the melts were cooled down to room temperature by pouring on a steel plate. This way, pellets of up to 10 mm in diameter and 2 mm in thickness were obtained. For the investigation of the liquidus surface, the samples were characterized by metallography and PXRD.

The clathrate phase was obtained with high purity in the composition range $2.4 \leq x \leq 3.8$ after annealing the as cast samples at 1000 °C for 1 week in a tube furnace, followed by water quenching. For the annealing experiments, specimens were placed in a glassy carbon crucible and welded in a tantalum ampoule which was in turn sealed in an argon-filled quartz tube. The thermal stability at lower temperatures was investigated by further annealing at 800 °C, 600 °C and 500 °C from 1d up to 2 weeks.

Clathrate phase $Ba_{8-\delta}Ni_x\square_ySi_{46-x-y}$ with lower Ba and Ni content ($\delta = 0.1$; $1.6 \leq x \leq 1.7$) was obtained by fast cooling of the melts between two steel plates.[18] The cooling rate in this way is estimated to be 10^3 Ks^{-1}, as the samples were found to be at room temperature immediately after quenching. The reaction products contained large amounts of $BaSi_2$ and α-Si, which were removed by treatment with 3M HCl for 8 h and afterwards, by 1M NaOH for 8 h (Fig. S1).

2.2 Powder X-ray Diffraction. PXRD data were obtained using an X-ray Guinier diffraction technique (Huber G670 camera, Cu-$K\alpha_1$ radiation, $\lambda = 1.54056$ Å, graphite monochromator, $5° \leq 2\theta \leq 100°$, $\Delta 2\theta = 0.005°$). The reflection positions were determined by profile deconvolution and corrected by LaB_6 ($a = 4.15683(9)$ Å at 295(2) K) as internal standard, which was added to the samples in small amounts. The unit cell parameter was calculated from a least-square refinement with the WinCSD program.[19]

2.3 Single Crystal X-ray Diffraction. Room temperature single crystal X-ray data were collected with a rotating-anode diffractometer (RIGAKU Spider, Varimax optical system, Ag-$K\alpha$ radiation, $\lambda = 0.56087$ Å). A multi-scan absorption correction was applied during the data collection. For the crystal structure determination, full-matrix least-squares refinements were carried out with WinCSD program. Details related to the data collection and structure refinements are given in Table 1, atomic coordinates and thermal displacement parameters in Table 2.

2.4 Microstructure Analysis. Samples stable to air and moisture were embedded in epoxy resin substrate containing carbon fibers. Grinding was performed with silicon carbide abrasive grinding discs together with alcohol including lubricants. Polishing was done in steps by using different polishing discs

of micron sized diamond powders (6, 3, 0.25 μm) in paraffin. Air or moisture sensitive samples were polished in an Ar-filled glove box using hexane as lubricant. Phase analyses were carried out by using a Philips XL 30 SEM with integrated EDX spectrometer. The compositions of the clathrate phase were determined with a Cameca SX 100 WDX spectrometer using Ba_6Ge_{25} and NiSi as external standards for the determination of Ba, Ni and Si content. Optical microscope images were obtained by a light optical polarization microscope (Zeiss Axio Plan).

2.5 X-ray Absorption Spectroscopy. The X-ray absorption spectra of the clathrate-I phase in the system Ba – Ni – Si were determined close to the Ni *K*-edge (8333 eV). The spectra were recorded in transmission mode at the EXAFS beamline C of HASYLAB at DESY (EXAFS: Extended X-ray Absorption Fine Structure). Samples of 20 mg were ground into fine powders, mixed with B_4C and mounted in paraffin wax on an area of 1 cm^2 with Kapton foil. Wavelength selection was realized by means of Si (111) double crystal monochromator. The energy range 8150 eV < E < 9600 eV was scanned with an EXAFS program starting with constant energy step size ΔE = 0.2 eV / integration time t = 1 sec in the XANES region close to the Ni *K*-edge and a constant step size in reciprocal space with $\Delta k = \sqrt{(E\text{-}E_{Ni})} = 7 \times 10^{-3}$ Å^{-1} in the EXAFS region. In total, 660 points and an increasing integration time up to 5 sec at 9600 eV led to totals of 30 min per scan. The absorption behavior $\mu(E) = -\ln(I1/I0)$ were calculated from the measured intensities at ionization chamber C1 and C0 behind and in front of the sample and subsequent spectra evaluations based on the averaging on two successively measured spectra. The energy values of the measured spectra were calibrated by means of the first inflection point of the simultaneously measured reference spectra (Ni-foil) (E_{Ni} = 8333 eV). EXAFS data analyses were performed using IFEFFIT program package.[20-22] Normalization of the absorption spectra $\mu(E)$ and the extraction of the EXAFS interference function $\chi(k)$ was performed with standard procedure which includes pre- and post-edge background removal. The applied cut-off value is given by R = 1.17 Å which is close to half of the expected distance to the next nearest neighbor of the Ni atoms (Ni–Si ≈ 2.3 Å). The EXAFS oscillations were multiplied by a scaling factor k^2 to enhance the features at higher k values.

2.6 Thermal Analysis. Thermal properties of the samples were investigated with a Netzsch DSC 404 C instrument. Bulk pieces of about 30 mg were transferred to a glassy carbon crucible (∅ = 4 mm, l = 6 mm, Sigradur G, HTW) which was then sealed in a Nb crucible (∅ = 5 mm, 600 mg). The system was heated under Ar atmosphere from room temperature up to 1300 ºC applying different heating (cooling) rates of 2 - 10 ºC / min.

2.7 Calculation Procedures. First-principles electronic structure calculations within the local density approximation to the density functional theory were performed using the all-electron, full-potential local orbital method (FPLO).[23] Perdew-Wang parametrization of the exchange-correlation potential was employed.[24] The calculations for $Ba_8Ni_x\square_ySi_{46-x-y}$ covered the compositions (x = 0 - 4, 6; y = 0) and (x = 3, 4; y = 1). In order to compute heats of formation and assess the stability of the clathrate phase, total energy calculations for the elemental solids (bcc Ba,[25] ferromagnetic fcc Ni, [25] and α-Si [25]), $BaSi_2$,[26] NiSi,[27] and $NiSi_2$ [28] were also carried out. The crystal structures of all these compounds were fully-optimized. In regard to the clathrates, however, only the end-members (x = 0 and 6; y = 0) were fully-optimized, while for the other compositions experimentally determined values of the structural parameters were used. Although the title compounds are found to crystallize in the space group $Pm\bar{3}n$, all Ni-containing members show disorder involving the 6*c* position (as discussed in the crystal structure part, see section 3.5.1, this is the site where Ni and Si atoms together with vacancies are located). We have chosen to model this chemical disorder by using supercells which are constructed according to the group-subgroup relations. The details regarding this matter were explained in a recent publication.[17]

The chemical bonding and charge transfer investigations were performed by combining the topological analysis of the electron localizability indicator (ELI) [29] and electron density (ED). Both ELI and ED were calculated by the FPLO method;[30] their topological analyses were carried out by the program Basin.[31]

2.8 Physical Properties Measurements. Electrical resistivity and thermopower were measured simultaneously in the 300 – 773 K temperature range using a commercial setup (ZEM-3, Ulvac-Riko). For the measurement, samples were cut from ingots to typical dimensions of 2 × 2 × 6 mm^3 using a

diamond-wire saw. Thermal conductivity λ was derived from thermal diffusivity, α, measured from 300 K up to 773 K using a Netzsch LFA 427 apparatus. The measurements were performed on square-shaped samples of 6 × 6 × 1 mm^3. The thermal conductivity was then calculated via $\lambda = \alpha C_p \rho_v$ where C_p is the specific heat and ρ_v is the density of the samples. The specific heat was considered to be constant and equal to the Dulong-Petit value throughout the temperature range investigated. No corrections for thermal dilatation were applied.

The superconductivity of the clathrate phase for low Ni contents was characterized by electrical resistivity measurements in the 2 – 10 K temperature range, using the AC option of a physical property measurements system (PPMS, Quantum Design). Copper wires were used as contacts and attached to the samples using a tiny amount of silver paint. Samples at this composition were prepared as fine powders. The measurements were performed on rods of 1.5 × 1 × 6.7 mm^3 obtained at 300 °C and 0.5 GPa.

3. RESULTS AND DISCUSSION

3.1 Liquidus Surface in the System $BaSi_2$ – NiSi – α-Si. A clathrate-I phase with the composition $Ba_8Ni_{1.8}Si_{44.2}$ was originally synthesized from a sample with nominal composition '$Ba_8Ni_6Si_{40}$'.[16] A polycrystalline product was obtained by heating up the sample in a corundum crucible to the melt, followed by cooling with 100 °C / h to room temperature. The composition was established from single crystal analysis. The homogeneity of the reaction product was not discussed, but due to differing compositions of starting material and clathrate phase, a multiphase product would be expected.

For both compositions, we obtained a multi-phase clathrate product by cooling down the melt within several minutes to room temperature. In order to understand the formation of the clathrate phase, we have investigated the liquidus surface of the system $BaSi_2$ – NiSi – α-Si which constitutes a subtriangle of congruently melting phases in the ternary system Ba – Ni – Si (Fig.1). For the binary system $BaSi_2$ – Si, an eutectic point has been reported at 83 at-% Si (Fig. 1, point ε_1),[32] while the binary system NiSi – Si has an eutectic point between NiSi and $NiSi_2$ at 56 at-% Si (Fig. 1, point ε_2).[33] The tie line of the

assumed phase triangle was confirmed from a sample with nominal composition "$BaNiSi_3$". PXRD pattern of the sample showed only reflections of $BaSi_2$ and NiSi comprising a mixture of finely divided crystallites in the microstructure (Fig. 2a). Hence, we assign the eutectic point of the quasibinary system $BaSi_2$ – NiSi to be close to the composition 20 at-% Ba, 20 at-% Ni, 60 at-% Si. According to DSC, the melting point was determined to be ≈ 920 °C at this composition (Fig. 1 point ε_3, Fig. S2). With three binary eutectic points, the liquidus surface of the system $BaSi_2$ – NiSi – α-Si is divided by cotectic lines in three regions. Our results show that the liquidus surfaces for $BaSi_2$ and NiSi reach both the corresponding cotectic tie lines, whereas the region towards α-Si is divided into the liquidus surfaces of α-Si, $NiSi_2$ and clathrate-I phase.

3.1.1 Liquidus Surfaces of α-Si, $NiSi_2$ and Clathrate-I. Initially, we investigated a composition row $Ba_8Ni_xSi_{46-x}$ ($0.2 \leq x \leq 10$), comprising the homogeneity range assumed for the clathrate-I phase. For x = 0.5 (Fig. 1, point 1), microstructure analysis showed large and well-shaped crystallites of the primary phase α-Si (Fig. 2b). On further cooling the silicon content of the melt is reduced and the cotectic line between α-Si and $BaSi_2$ is reached leading to smaller, but still distinctly shaped crystals of $BaSi_2$ and α-Si. When the Ni content of the melt becomes high enough, a common crystallization of $BaSi_2$ and clathrate phase (instead of α-Si) sets in. The ternary eutectic point could not be identified for Ni concentrations $x \leq 0.5$. For a sample with slightly higher Ni-content, $Ba_{10}Ni_2Si_{88}$ (Fig. 1, point 2), the cotectic line of $BaSi_2$ and α-Si cannot be reached any more on crystallization of α-Si. Instead, the liquidus surface of clathrate phase is reached and both large crystallites of α-Si and clathrate phase are found in the microstructure (Fig. 2c). On crystallization, the clathrate crystals totally envelope the α-Si crystals, till the cotectic crystallization of $BaSi_2$ and clathrate phase sets in. Hence, for the primary crystallization field of clathrate phase the limit toward lower Ni contents can be estimated from a projection line drawn from α-Si in between point 1 and point 2. For higher Ni concentrations x = 3 and x = 4 (Fig. 1, points 3 and 4) crystals of the primary phase α-Si are entirely enveloped by clathrate phase (Fig. 2d, Fig. S3a). Due to relatively smaller amount of α-Si for x = 4, we consider this point to be close

to the liquidus surface of clathrate-I phase. On precipitation of clathrate phase, the cotectic line of clathrate phase and $BaSi_2$ is reached running towards the ternary eutectic point. The ternary eutectic of $BaSi_2$, NiSi and clathrate phase was identified with a composition of around 8 at-% Ba, 34 at-% Ni, 58 at-% Si (Fig. 1, point τ). For samples with $x = 6$ and $x = 10$ (Fig. 1, points 5 and 6), well-shaped crystallites of clathrate-I phase form primarily (Fig. 2e, Fig. S3b), which explains, why single crystals suitable for structure investigations could be obtained in earlier work,[16] from the melt at composition $x = 6$. The microstructure of both samples also show crystallites of $BaSi_2$, which are formed on cotectic precipitation. No α-Si is detected any more in both microstructure and PXRD. The presence of NiSi was proven by PXRD (Fig. S4), as the size of NiSi grains within the eutectic part of the microstructure was too small to be analyzed separately by SEM. The border between the clathrate-I and α-Si liquidus surfaces was estimated from two groups of samples: For the compositions $x = 6$ and $Ba_{10}Ni_{20}Si_{70}$ (Fig. 1, points 5 and 9, Fig. S3c), clathrate-I phase was the primary phase, whereas for the compositions $x = 4$, $Ba_5Ni_{20}Si_{75}$ and $Ba_5Ni_{30}Si_{65}$ (Fig. 1, points 4, 7 and 8, Fig. 2e, Fig. S3d-d1, Fig. 2f-f`1), α-Si was primarily formed from the melt. For the composition $Ba_5Ni_{30}Si_{65}$ (Fig. 1, point 8), crystals of α-Si are formed as primary phase, which are almost entirely enveloped by $NiSi_2$ (Fig. 2f-f1). On crystallization of $NiSi_2$, the liquidus surface of clathrate is reached. Now, both phases are formed with well-shaped crystals till the cotectic line between clathrate and NiSi is reached. This is represented in the microstructure by areas with a finely grained mixture of NiSi and clathrate phase and the presence of all mentioned phases in PXRD pattern. The primary crystallization field of $NiSi_2$ was not investigated in detail in this work.

3.1.2 Liquidus Surface of $BaSi_2$. The primary crystallization field of $BaSi_2$ is shown for a sample with composition $Ba_{25}Ni_5Si_{70}$ (Fig. 1, point 10). In the microstructure, large crystals of the primary phase $BaSi_2$ are surrounded by clathrate phase (Fig. 2g). The presence of NiSi, which is formed at eutectic composition, was only observed by PXRD (Fig. S5). A sample at the cotectic line between $BaSi_2$ and clathrate phase was obtained for the composition $Ba_{20}Ni_{10}Si_{70}$ (Fig. 1, point 11). Small crystallites of both clathrate phase and $BaSi_2$ are formed, similar in shape and amount (Fig. 2h). The

composition $Ba_{12}Ni_{30}Si_{58}$ represents the upper limit of the $BaSi_2$ liquidus surface (Fig. 1, point 12). $BaSi_2$ crystallites are formed primarily till the cotectic line of $BaSi_2$ and NiSi, and finally the ternary eutectic is reached (Fig. 2i).

3.1.3 Liquidus Surface of NiSi. The primary crystallization field of NiSi is shown for a sample with composition $Ba_5Ni_{40}Si_{55}$ (Fig. 1, point 13). On crystallization of large and isolated crystals of NiSi, the cotectic line between NiSi and $BaSi_2$ is reached, indicated by a mixture of $BaSi_2$ and NiSi crystallites (Fig. 2j). Fine coarse areas with eutectic microstructure between $BaSi_2$, clathrate phase and NiSi are visible (Fig. 2j1). The clathrate phase was unambiguously identified by PXRD (Fig. S6).

3.2 The Homogeneity Range of the Clathrate Phase

3.2.1 Isothermal Section of the System $BaSi_2$ – NiSi – α-Si at 1000°C. As discussed in the previous section, only multiphase products can be formed on cooling ternary mixtures from the melt. A homogeneous clathrate phase $Ba_8Ni_x\square_ySi_{46-x-y}$ with $2.4 \leq x \leq 3.8$ and $y \leq 0.8$ was obtained after annealing at 1000 °C for 1 week. In the ternary system $BaSi_2$ – NiSi – α-Si, the melting points of NiSi, $NiSi_2$, the quasi-binary eutectic "$BaNiSi_3$" and the ternary eutectic are below 1000 °C (Fig. 1). Therefore, samples with higher Ni content are either entirely molten or solid phases are in equilibrium with melt (Fig. 3a). Of the latter case, three different regions should occur in which either $BaSi_2$ and clathrate-I, or clathrate-I and α-Si, or only clathrate-I are present as precipitate. For lower Ni content, three sections with solid state equilibria are present, two-phase regions of clathrate-I with $BaSi_2$ and clathrate-I with α-Si, and a three-phase region of clathrate-I, $BaSi_2$ and α-Si.

The three-phase region is represented by samples with the compositions $Ba_8Ni_{0.5}Si_{45.5}$ (Fig. 3a, P1), $Ba_8Ni_{2.0}Si_{44}$ (Fig. 3a, P2), $Ba_{22.5}Ni_{2.5}Si_{75}$ (Fig. 3a, P3) and $Ba_{10}Ni_2Si_{88}$ (Fig. 3a, P4). The microstructure of each sample shows well separated crystallites of $BaSi_2$, α-Si and clathrate phase in the respective amounts (Fig. 4a, Fig. S7a-c). The clathrate composition of $Ba_8Ni_{2.4}Si_{43.9}$ was determined from point 2 (Table 3) and represents the lower limit of Ni in the homogeneity range of clathrate at 1000 °C. The two-phase regions are represented by samples with the compositions $Ba_{18}Ni_5Si_{77}$ (Fig. 3a, P5) and

$Ba_{13}Ni_5Si_{82}$ (Fig. 3a, P6) showing a mixture of $BaSi_2$ and clathrate phase (Fig. 4b) or α-Si and clathrate phase (Fig. 4c), respectively. The phase mixtures obtained for samples with composition $Ba_{25}Ni_5Si_{70}$ (Fig. 3a, P7) and $Ba_{2.5}Ni_{2.5}Si_{95}$ (Fig. 3a, P8) belong to three-phase regions in equilibrium with melt (Fig. S7d-e). For the composition $Ba_8Ni_{4.0}Si_{42.0}$ (Fig. 3a, P9) only the clathrate phase should be in equilibrium with a small amount of melt. Accordingly, the microstructure shows large homogeneous grains of clathrate phase surrounded by finely grained mixture crystallized from the melt when the sample was cooled from 1000°C to room temperature (Fig. 4d). The composition $Ba_8Ni_{3.8}Si_{41.3}\square_{0.9}$ of the clathrate phase represents the upper limit of Ni content in the phase range (Table 3).

A more detailed analysis of the homogeneity range of the clathrate phase at 1000 °C is based on a variety of samples with nominal compositions $Ba_8Ni_xSi_{46-x}$ ($0 < x < 10$) (Table 3). Assuming this formula is valid, the clathrate phase should have the same Ba content within the whole composition range (Fig. 3b, dotted line). However, the composition of the clathrate phase determined from WDXS is shifted towards higher Ba and Ni contents with increasing content of Ni in the starting material. For lower Ni content, the deviation from the composition range $Ba_8Ni_xSi_{46-x}$ is still within experimental error of WDXS analysis, whereas for higher Ni content the formula clearly cannot describe the compositions from WDXS analysis. Clathrates with higher Ba content can only be explained by the presence of vacancies □ in the framework, which cannot host more than 8 Ba-atoms. In fact, the metallography results point to a homogeneity range $Ba_8Ni_x\square_ySi_{46-x-y}$ with $y \geq 0$ for the clathrate-I phase at 1000 °C.

3.2.2 Synthesis by fast cooling. The compositions accessible by fast cooling can differ from those of equilibrium samples at a certain annealing temperature for kinetic reasons. Moreover, the crystallization temperature of the clathrate phase is not known, because supercooling of the melt can hardly be controlled in the experiment. On the other hand, by pouring the melt on a steel plate, the cooling rate is in many cases sufficiently high to avoid the decomposition of high-temperature phases at temperatures just below the limit of the stability range. After annealing, such phases can decompose on cooling sealed ampoules with conventional techniques, e.g. water quenching. As discussed for the liquidus surface, we

did not obtain directly a pure clathrate phase by quenching of melt droplets on a steel plate, because the rapid crystallization of α-Si could not be suppressed. Phase pure samples could only be obtained in equilibrium after annealing at 1000°C.

However, in order to analyze the clathrate phase directly formed after fast cooling, $BaSi_2$ and α-Si were removed from the product by treatment with dilute HCl and NaOH. For samples with nominal compositions $Ba_8Ni_{0.2}Si_{45.8}$ and $Ba_8Ni_{0.5}Si_{45.5}$, structure analysis by powder X-ray diffraction combined with EDXS results revealed the compositions $Ba_{7.9}Ni_{1.6}Si_{44.4}$ and $Ba_{7.9}Ni_{1.7}Si_{44.3}$, respectively (Table 4). After 1 d annealing at 1000 ºC, $Ba_{7.9}Ni_{1.7}Si_{44.3}$ partially decomposed to clathrate phase with composition $Ba_8Ni_{3.4}Si_{42.6}$, α–Si and an unidentified phase. Obviously, the Ba and Ni contents of the clathrate phase obtained by fast cooling can be significantly lowered compared to their content in the samples obtained at 1000 °C. Clathrates showing Ba deficiency were not obtained in samples with higher Ni content, the compositions of which correspond to the homogeneity range at 1000 °C. For example, starting from nominal composition $Ba_8Ni_{3.5}Si_{42.5}$, the clathrate phase was obtained with composition $Ba_{8.0}Ni_{3.0}Si_{42.3}$. These results point to a broader homogeneity range for the clathrate phase at temperatures different from 1000 °C.

3.3 Thermal stability of clathrate-I phase. Clathrate products obtained at 1000 °C with $2.4 < x < 3.8$ were investigated by heat-flux DSC experiments. The melting temperature of pure clathrate phase was found to be 1105 °C and does not change significantly by composition within experimental error (Fig. S8). All samples show only one thermal effect on heating and in accordance with the liquidus surface, several characteristic effects on cooling. At temperatures lower than 1000 °C, the homogeneity range narrows to compositions with higher Ni content. A sample with composition $Ba_8Ni_{3.5}Si_{42.5}$, which was obtained in thermal equilibrium at 1000 °C was further annealed at 800 °C and 600 °C. After two weeks at 800 °C, the lattice parameter of the clathrate phase decreased from a = 10.2904(1) Å to a = 10.28920(8) Å, at 600 ºC to a = 10.2877(1) Å (Fig. S9). Both lattice parameters are smaller than that for the composition $Ba_8Ni_{3.8}Si_{41.3}$ (a = 10.2896(1) Å), representing the highest Ni content of the clathrate phase at 1000°C. As the Ba positions of the clathrate phase were found to be fully occupied by structure

refinements on powder (see section 3.5.1) the results are consistent with a higher Ni content of the clathrate phase.

Clathrates with low Ni and Ba content, formed by splat cooling and purified by washing out the byproducts, are metastable according to heat-flux DSC experiments. Phase pure sample of $Ba_{7.9}Ni_{1.7}Si_{44.3}$ showed an exothermic effect on heating with 10 K/min at ≈ 715 ºC (Fig. S10). After cooling to room temperature, the sample consisted of α-Si, a clathrate-I phase with smaller lattice parameter and an unidentified phase. The same product was obtained for a sample annealed for 1 day at 800 °C. At 500 ºC, the metastable clathrate phase decomposes differently. After 1 d annealing, two different clathrate-I compounds (a = 10.3047(3) Å and a = 10.2890(3) Å) and small amounts of α-Si were formed. Further annealing for 2 d increased the content of the clathrate phase with smaller lattice parameter. The complex phase relations in the system Ba – Ni – Si at lower temperatures are subject of ongoing investigations.

3.4 Heats of Formation and Phase Stability. The heats of formation of $Ba_8Ni_x\square_ySi_{46-x-y}$ is calculated by considering the following reaction:

$$8Ba\ (bcc) + xNi(fcc;\ FM) + (46\text{-}x\text{-}y)\ \alpha\text{-}Si \rightarrow Ba_8Ni_x\square_ySi_{46-x-y} + \Delta H_f(x, y) \qquad \text{(Eq. 1)}$$

Additionally, the stability of the clathrate phase with respect to the competing phases is explored through electronic total energies. The decomposition products as determined by phase diagram studies and WDXS analyses are taken as the competing phases. They are $BaSi_2$, NiSi and α-Si for $x \leq 3$, while for $x > 3.5$ $NiSi_2$ is also observed. When both NiSi and $NiSi_2$ are present, however, their relative weights cannot be determined uniquely. Therefore, we take into account only NiSi in computing the energy differences for all x values, and comment on the effect of $NiSi_2$ for the x = 4 case separately. The decomposition reaction considered is

$$Ba_8Ni_x\square_ySi_{46-x-y} \rightarrow 8\ BaSi_2 + x\ NiSi + (30 - 2x - y)\ \alpha\text{-}Si + \Delta E(x, y) \qquad \text{(Eq. 2)}$$

The results for both $\Delta H_f(x, y)$ and $\Delta E(x, y)$ are presented in Table 5 according to (x, y) pairs. Their variation with Ni content for the y = 0 case (no vacancy) is plotted in Fig. 5. We observe that ΔH_f varies

linearly with Ni content with two different slopes in the ranges $0 \leq x \leq 3$ and $3 \leq x \leq 6$. This observation is another example of the claim stated earlier that the composition corresponding to $x = 3$ is special in the sense that it delineates two regions of different behavior.[17] In the current context, this means that the additional energy saved upon forming a clathrate with one more Ni atom per formula unit for x up to 3 is almost twice that for $x > 3$ (~25 meV atom^{-1} versus ~14 meV atom^{-1}). Both vacancy models have lower heats of formation implying that for the $x = 3$ and 4 cases vacancies are not preferred. In fact, the vacancy formation energies computed by using the following reactions:

$$Ba_8Ni_3Si_{43} \rightarrow Ba_8Ni_3Si_{42} + \alpha\text{-Si} + \Delta E_v \qquad \text{(Eq. 3a)}$$

$$Ba_8Ni_4Si_{42} \rightarrow Ba_8Ni_3Si_{41} + \alpha\text{-Si} + \Delta E_v \qquad \text{(Eq. 3b)}$$

are –1.40 and –1.62 eV for one vacancy per formula unit for $x = 3$ and 4, respectively, leading to the result that internal energy contributions alone would prefer $Ba_8Ni_3Si_{43}$ and $Ba_8Ni_4Si_{42}$. The entropy contributions due especially to phonons may eventually favor presence of vacancies at 6*c* position at elevated temperatures. Such calculations will be the subject of future studies.

Negative values of $\Delta E(x, y)$ indicate that clathrate phase is more stable than the decomposition products. Examination of Table 5 and Fig. 5 reveals two clear results: **(i)** all clathrates with $x \leq 3$ are stable, the $x = 3$ clathrate being the most stable one, **(ii)** $Ba_8Ni_6Si_{40}$ ($x = 6$) is unstable in agreement with the fact that this compound has not been observed yet. The former result can be understood using the heats of formation results. Since after three Ni atoms, addition of an extra Ni atom saves less energy, the competing phases quickly become more favorable for $x > 3$. The chemical reason behind this result is probably the tendency for avoiding two Ni atoms at the 6c sites of the same six-ring substructure. The not-so-clear result involves the $x = 4$ case. Eq. 2 using only NiSi predicts that $Ba_8Ni_4Si_{42}$ is stable. Since, however, $NiSi_2$ is calculated to have a higher heat of formation than NiSi, if it is included among the competing phases, ΔE may change sign. In fact, a small amount of $NiSi_2$ is sufficient for that, ΔE ($x = 4$) is ~ 0 meV atom^{-1} when the right-hand-side of Eq. 2 contains 0.4546 $NiSi_2$ and 3.5454 NiSi. Unfortunately, the indeterminancy in the NiSi and $NiSi_2$ concentrations on the decomposition side of the

equation prevents a clear statement to be made about the stability of $Ba_8Ni_4Si_{42}$. Furthermore, as mentioned above, there is also the issue of the vacancies and the associated entropy contributions to the free energy for x in the vicinity of 4, which adds more uncertainty to the problem. Note that, Eq. 2 predicts that both vacancy cases are unstable.

3.5 Crystal Structure.

3.5.1 Single Crystal Analyses. X-ray powder patterns of all clathrate-I products could be indexed with a primitive cubic lattice in agreement with the space group $Pm\bar{3}n$ (no. 223). A supercell indicating an ordered arrangement of Ni atoms or defects in the clathrate-I framework was not observed.[18] As the reflections in all powder patterns were distinctly narrow, it was assumed that the bulk composition determined by WDXS is also valid for the single crystalline fragments.

The clathrate-I structure is represented in space group $Pm\bar{3}n$ by two crystallographic sites for cage atoms (2*a*, 6*d*) and three for framework atoms (6*c*, 16*i*, 24*k*) (Fig. 6). However, the crystallographic sites describe only averaged positions because the local crystal structure of clathrates can be distorted by mixed-occupancy sites and vacancies. Such features are often indicated by unusual thermal displacement parameters. While the presence of vacancies is indicated by large values of isotropic displacement parameters U_{iso}, closely adjacent split sites are expressed by large anisotropy U_{ij}. The latter one could be resolved with single-crystal data sets collected to sufficiently high diffraction angles.[34]

The arrangement of substitution atoms and defects in heteroatomic clathrate-I frameworks can be understood from the connectivity pattern. The framework consists of 4-bonded atoms connected to twisted pentagons and planar hexagons, which enclose the characteristic 20-atom [5^{12}] polyhedra centered by 2*a* site and 24-atom [$6^2 5^{12}$] polyhedra centered by 6*d* site. The hexagons formed by atoms at 6*c* and 24*k* sites are connected via common 6*c* atoms to infinite chains along <100>. The atoms at 6*c* sites join two hexagons with 120° bond angles so that the coordination environment is especially unfavorable for 4-bonded Si atoms. Hence, defects or substitution atoms are preferentially found at this

site. Considering that the 16*i* and 24*k* sites are fully occupied by Si atoms, reliable scaling for the electron density at 6*c* site is obtained from crystal structure refinement. However, when Si atoms, substitution atoms and vacancies share the same site, the electron density value fits a range of possible occupancies. Hence, the chemical composition can only be revealed by combining the results of the structure refinement and elemental analysis.

Crystal structure determinations were performed on three single crystals selected from 1000° C annealed samples with WDXS compositions $Ba_8Ni_{2.6}Si_{42.6}$, $Ba_8Ni_{3.2}Si_{43.0}$ and $Ba_8Ni_{3.7}Si_{41.8}$. The structure refinements reveal in all cases full occupancy of Ba1 atoms at 2*a* (0, 0, 0) and Ba2 atoms at 6*d* (1/4, ½, 0). On the other hand, Ba2 atoms in oversized 24-atom cages show plate-like ellipsoids which can be assigned to presence of off-centered positions.[35, 36] If Ba2 atoms are refined at the 24*k* split site (*x*, *y*, 0) with 0.25 occupancy, the residual values are considerably lowered (i.e. R_F for $Ba_8Ni_{2.6}Si_{42.6}$ drops from 3.9 % to 3.0 %). In the initial structure models, the framework vacancies were not considered. For the framework site 6*c* (1/4, 0, ½), the Ni to Si ratio was refined for full site occupancy, while sites 16*i* (*x*, *x*, *x*) and 24*k* (0, *y*, *z*) were refined with full Si occupancy. The number of Ni atoms per formula unit was refined to be 2.5, 2.9 and 3.1 which did not match to the values 2.6, 3.2 and 3.7, respectively, obtained from WDXS analyses. The discrepancy increasing towards higher Ni content can only be explained by presence of vacancies at the 6*c* site. Differently to Si atoms at 16*i* site, atoms at 24*k* site show slightly increasing U_{ij} values with increasing Ni content. This sizable anisotropy in 24*k* site was correlated with the amount of vacancies as observed for binary clathrate-I $K_8Ge_{44}\square_2$,[37] and $Cs_8Sn_{44}\square_2$[38] as well as for ternary clathrate-I compounds with transition metals, $Ba_8TM_xGe_{46-x-y}\square_y$ (*TM* = Ni,[34] Pd,[39] Pt,[40] Zn[41, 42] etc.).

For $Ba_8Ni_{2.6}Si_{42.6}$, the single crystal refinement with fixed Ni content of 2.6 atoms per unit cell gives 3.3 Si atoms at 6*c* site with remaining ~0.1 vacancies. In the same way, 2.4 and 1.4 Si atoms are found at 6*c* with respective vacancies of ~0.4 and ~0.9 for $Ba_8Ni_{3.2}Si_{43.0}$ and $Ba_8Ni_{3.7}Si_{41.8}$. The structure

refinements, thus, yield the compositions $Ba_8Ni_{2.6}Si_{43.3}$, $Ba_8Ni_{3.2}Si_{42.4}$ and $Ba_8Ni_{3.7}Si_{41.4}$ for the investigated single crystals. To correlate the mixed occupancy at 6*c* site with 24*k* site, the mean electron density around 24*k* site for $Ba_8Ni_{2.6}Si_{42.6}$ was approximated by two Si positions as Si31 (neighbor of Si at 6*c*), Si32 (neighbor of Ni at 6*c*) and for $Ba_8Ni_{3.2}Si_{43.0}$ and $Ba_8Ni_{3.7}Si_{41.8}$ by three Si positions as Si31, Si32, and Si33 (neighbor of vacancy at 6*c*). We obtained self-consistent data sets by repeatedly refining the coordinates, the atomic displacement parameters and the occupancies (except for Ni and Ba) until good agreement between the structure model and the experimental data was obtained (low R_F values). The results are tabulated in Table 1 and 2.

The formation of vacancies leads to a relaxation of the neighboring atoms, which are shifted towards the defect position. In the case of $Ba_8Ge_{43}\square_3$ in which the defects are ordered to form a super structure, the distances between atoms at sites 6*c* and 24*k* were accurately determined to be d(Ge1 – Ge3) ≈ 2.5 Å and d(□ – Ge3) ≈ 2.2, respectively.[18] Hence, for a Ge framework the difference amount to ≈ 0.3 Å. For vacancy containing Si clathrates, which have not been paid much attention to in the literature, the difference between the corresponding distances is considered to be slightly smaller.

Introducing a split atom model for clathrate-I $Ba_8Ni_x\square_ySi_{46-x-y}$, we find that the distances between 6*c* and neighboring 24*k* sites are d(Si1 – Si3) ≈ 2.4 Å , d(Ni1– Si3) ≈ 2.3 and d(□ – Si3) ≈ 2.2. The interatomic distances d(Si1 – Si31) from single crystal data varying in the range 2.40 Å – 2.46 Å are slightly longer than the Si – Si distance in α-Si (2.35 Å) (Tables S1-S3) but agrees well with those in other clathrates e.g. $Na_2Ba_6Si_{46}$ (≈ 2.40 Å),[43] or $Cs_{7.8}Si_{46}$ (≈ 2.44 Å) [44] . The distances for d(Ni – Si32) ≈ 2.28 Å – 2.33 Å are in the range with those reported in NiSi as d(Ni – Si) ≈ 2.29 - 2.40 Å,[45] or in $NiSi_2$ as d(Ni-Si) ≈ 2.34 Å.[28] Distances d(□ – Si33) ≈ 2.15 Å – 2.19 Å are close to d(□ – Ge) ≈ 2.14 – 2.18 Å reported for $Ba_8Ge_{43}\square_3$.[18]

As refined from the PXRD data, the lattice parameter of the clathrate phase decreases with increasing Ni content, c.f. a = 10.3088(1) Å for $Ba_{7.9}Ni_{1.6}Si_{44.4}$ and a = 10.2896(1) Å for $Ba_8Ni_{3.8}Si_{41.3}$ at the lower and upper limits of the homogeneity range, respectively (Fig. 7). This may be explained by small

contraction of the framework as the Ni-Si3 interatomic distances ($d_{Ni1\text{-}Si3} \approx 2.28$ Å – 2.33 Å) are slightly shorter than those of the Si1-Si3 in the parent compound Ba_8Si_{46} ($d_{Si1\text{-}Si3} \approx 2.42$Å, $a = 10.328(2)$ Å).[5]

3.5.2 Rietveld Refinements of Fast Cooled Samples. Ba deficiency of the fast cooled samples with nominal compositions $Ba_8Ni_{0.2}Si_{45.8}$ and $Ba_8Ni_{0.5}Si_{45.5}$ was verified by the Rietveld refinements. The Ni content was fixed to the value which was obtained from the EDXS analyses. The Ba1 site was found to be partially occupied. On the other hand, the Ba2 site as well as the framework sites are fully occupied. Accordingly, the compositions of $Ba_8Ni_{0.2}Si_{45.8}$ and $Ba_8Ni_{0.5}Si_{45.5}$ were determined to be $Ba_{7.9}Ni_{1.6}Si_{44.4}$ and $Ba_{7.9}Ni_{1.7}Si_{44.3}$, respectively, from a combined EDXS and Rietveld analyses. To check if Ba deficient samples can be also synthesized for clathrates with higher Ni content, a sample with nominal composition $Ba_8Ni_{3.5}Si_{42.5}$ was fast quenched. The composition was determined with EDXS analysis as $Ba_{8.0}Ni_{3.0}Si_{42.3}$. From the Rietveld analysis, both Ba1 and Ba2 sites were found to be fully occupied but 6*c* site (1/4, 0, 1/2) on the framework shows around 0.4 vacancy per formula unit which is slightly smaller than 0.7, determined from the EDXS analysis.

3.6 X-ray Absorption Spectroscopy Measurements. X-ray absorption spectra of the clathrate phase in the system Ba – Ni – Si have been determined close to the Ni *K*-edge (8333 eV) on four samples with different nominal Ni content $x = 2.5$, 3.0, 3.5, and 4.0 (Fig. 8a). In addition, the XAS of Ni foil, NiSi, NiI_2 and NiO were recorded for comparison (Fig. 8b). According to the XAS measurements, the Ni *K*-edge XANES and EXAFS regions of clathrate samples with different Ni content show qualitatively identical features. The position of the absorption edge in the investigated clathrate compounds was found to be very close to those of Ni foil and NiSi and distinctly separated from those of NiI_2 and NiO. It was reported by several studies dealing with Ni compounds that the energy of the X-ray absorption edge correlates well with the variation of Ni valency and shifts to higher values as the valency increases.[46, 47] This behavior is also observed in our experiments, as the position of the edge region is shifted to higher energies with increasing oxidation state of Ni from 0 to +2. Accordingly, the oxidation state of Ni in investigated clathrate compounds is considered to be close to 0. As depicted in Fig. 8a, the

spectra of clathrates near the Ni *K*-edge exhibit distinct features which are dominated by the dipole transition of the 1*s* electron to unoccupied 4*p* states of the Ni atom.

Multiple-scattering effects govern the spectra at higher energies and lead to modulations in the EXAFS region of the spectra. Subtracting the smooth, step-like background extracts the modulation which is shown in the k^2-weighted presentation in Fig. 9. A detailed analysis of the EXAFS data shows almost identical features for all samples pointing to very similar local environments. While the major peak in the Fourier-transformed curve reflects the tetrahedral environment of the absorbing Ni atom which is formed by Si atoms with d(Ni–Si) ≈ 2.2 Å, the broad peak at around 3.7 Å is associated to the Ni – Ba2 interactions.

3.7 Chemical Bonding Analysis. The atomic interactions in the $Ba_8Ni_x\square_ySi_{46-x-y}$ system are studied within the ELI-ED approach by considering exemplarily its two members $Ba_8Ni_4Si_{42}$ and $Ba_8Ni_6Si_{40}$. Topological analysis of the ED enables to define atomic regions in molecules or solids in a unique way, so that charge transfer issues can be addressed on a firmer ground.[48] Similarly, topological analysis of ELI reveals the bonding situation in a molecule or solid by determining the local maxima of the ELI, called attractors, and the associated basins of the attractors. In addition, the deviation of the ELI distribution from the spherical one in the penultimate shell of an atom (referred to as structuring) also indicates the participation of the electrons of that shell in chemical bonding.

In $Ba_8Ni_4Si_{42}$, the computed atomic charges are as follows: 54.8 electrons for Ba1, 54.7 for Ba2, 28.4 for Ni, 14.1 for Si1 and 14.2 for Si2. Si3 atoms can be grouped into two according to being nearest neighbors of (i) Ni and (ii) Si1 atoms. The former group has 14.1 and the latter 14.3 electrons. This analysis shows that Ni atoms receive quite a large part (0.4 electrons per atom) of the electrons transferred from Ba atoms to the framework.

Topological analysis of the ELI reveals two-electron two-center type Si-Si and two-center banana-type Ni-Si bonds in the valence region. The electron counts inside typical bond basins can be summarized as follows: Ni-Si3: 2.2, Si1-Si3: 2.1, Si2-Si2: 2.0, Si3-Si3: 2.0. The Si2-Si3 bond charges

show a small difference depending on whether the Si3 atom is a neighbor of a Ni or Si atom, but essentially the electron count is 2.0 in both basins. We observe that the largest valence bond electron populations are obtained for the (6*c*)-Si3 bonds suggesting that excess valence charge tends to accumulate near the 6c sites. Hence, isosurfaces of the ELI distribution around a six-ring containing (a) Ni-Ni, (b) Ni-Si pairs at its 6*c* positions are shown in Fig. 10.

Ba 5*d* orbitals hybridize with framework orbitals (mainly Si 3*p* and Ni 3*d*) and have sizable occupancies (0.8 and 0.6 electrons for Ba1 and Ba2, respectively, for $x = 4$). Since the ELI organizes the electrons according to the principal quantum number, the 5*d* electrons belong to the Ba core regions, and thus their participation to the bonding is expected to cause structuring of the penultimate shells ($n = 5$) of Ba1 and Ba2. The structuring of Ba2 penultimate shell is shown in Fig. 10c, but that of Ba1 is too weak for a clear depiction. Furthermore, the participation of Ni 3*d* orbitals in Ni-Ba and Ni-Si interactions gives rise to a clearly-observable structuring of the $n = 3$ shell (Fig. 10c).

3.8 Physical Properties.

3.8.1 Superconductivity. Fig. 11a presents the comparison of the low-temperature electrical resistivity $\rho(T)$ of the $Ba_{7.9}Ni_{1.6}Si_{44.4}$ and $Ba_{7.9}Ni_{1.7}Si_{44.3}$ samples. As can be seen, the ρ values remain quasi-constant down to the superconducting transition that starts with onsets at $T_c = 6$ and 5.5 K and drop to zero resistance by 3.5 and 3 K for the $x = 1.6$ and $x = 1.7$ samples, respectively. This indicates broad resistive transitions of $\Delta T_c \sim 2.5$ K for both compounds which may be related to inhomogeneities in the Ni content in these samples. In any case, X-ray diffraction measurements together with the EDXS analyses revealed no detectable impurity phase indicating that the superconducting transitions observed are an intrinsic property of the clathrate phase. The presence of Ni results in a slight decrease in T_c compared to Ba_8Si_{46} where a superconducting state sets in at 8 K (Fig. 11b). Further addition of Ni ($x = 2.4$) then results in a complete suppression of superconductivity down to 0.4 K as shown by low-temperature electrical resistivity measurements reported in detail elsewhere.[17] This sharp decrease in T_c reflects the evolution of the density of states at the Fermi level, $N(E_F)$, which shows only slight

variations for $0 \leq x \leq 2.0$ before exhibiting a drastic decrease between $x = 2.0$ and $x = 3.0$. Thus the decrease in the electron-phonon coupling strength in $Ba_{8-\delta}Ni_x\square_ySi_{46-x-y}$ originates from the Ni-content-dependent variations in the electronic band structure as discussed previously.[17] A decrease in T_c is a feature shared by all ternary type-I clathrates investigated so far showing that alloying on the Ba or Si site tends to suppress superconductivity. However, the variations in T_c strongly depend on the substituting element as found out in several studies on $Ba_8M_xSi_{46-x}$ for M = Ge,[6] Ga [7] or Cu.[8] While a superconducting state still develops in the Ge and Ga-substituted systems up to $x = 25$ and $x = 10$, respectively, a lower Cu content of $x = 4$ is sufficient to drop T_c from 8 K down to 2.9 K. In the present case, Ni has a stronger influence since superconductivity disappears above $x = 2.4$.

3.8.2 High Temperature Thermoelectric Properties. Fig. 12 shows the temperature dependence of the electrical resistivity of the five samples studied. The electrical resistivity of clathrate samples increases linearly with temperature indicative of a metallic-like behavior to reach values ranging between 3.5 and 5.9 μΩ.m at 750 K. The substitution of Si by Ni results in an increase of the electrical resistivity for $2.6 \leq x \leq 3.5$. At the maximum Ni content that can be achieved i.e. $x = 3.8$, the electrical resistivity values are slightly lower than those of the $x = 3.5$ sample.

The temperature dependence of the thermopower is shown in Fig. 13. Regardless of the composition, the thermopower values remain negative above room temperature indicating a dominant contribution from electrons. The metallic character of these samples results in moderate values that increase in absolute value with temperature to reach values ranging between –30 and –40 $\mu V.K^{-1}$ at 750 K. No clear trend of the thermopower values as a function the Ni content can be unraveled in these data. This behavior originates from a balance between the hole and electron contributions to the thermopower as shown by detailed investigations of the low-temperature transport properties revealing that both type of carriers are involved in the electrical conduction of these compounds.[17]

The temperature dependence of the thermal conductivity is depicted in Fig. 14a. The thermal conductivity values are weakly temperature dependent ranging between 4.0 and 6.5 $W.m^{-1}.K^{-1}$ at 800 K. The measured values decrease with increasing Ni content up to $x = 3.5$ and remain quasi-constant with

further addition of Ni. The observed behavior against x mainly reflects the variations of the electrical resistivity as evidenced by the temperature dependences of the lattice and electronic thermal conductivity displayed in Fig. 14b and 14c, respectively. To separate these two contributions, the electrical resistivity values were used to estimate the electronic contribution, λ_e, via the Wiedemann-Franz law $\lambda_e = LT/\rho$ where L is the Lorenz number. This parameter was assumed as a first approximation to be equal to the value of a degenerate electron gas $L = L_0 = 2.44 \times 10^{-8}$ $V^2.K^{-2}$. The lattice thermal conductivity values, λ_L, are coherent with those reported on other Si-based clathrates and decrease with temperature over the entire temperature range as expected from dominant phonon-phonon interactions. In addition, a decrease of λ_L occurs as the Ni concentration is increased.

The combination of the transport properties results in a maximum ZT value of around 0.1 at 700 K for the x = 3.8 sample. The metallic nature of these samples is the main reason for the low ZT values. Increasing the thermoelectric efficiency may be achieved by further adjustment of the carrier concentration which may be realized through partial substitution of framework atoms by e.g. Ga or Al.

4. CONCLUSIONS

Type-I clathrates $Ba_{8-\delta}Ni_x\square_zSi_{46-x-y}$ have been prepared by steel-quenching as well as annealing at 1000 °C. A slightly Ba deficient compounds with low Ni content are obtained with the compositions $Ba_{7.9}Ni_{1.6}Si_{43.4}$ and $Ba_{7.9}Ni_{1.7}Si_{43.3}$ after steel-quenching. Homogeneity range for the annealed clathrate samples vary from x = 1.6 to 3.8. Single crystal analyses show that the clathrate phase crystallizes in the space group $Pm\bar{3}n$ in which the framework contains up to ~0.9 vacancies per unit cell for x = 3.7. The stability range of clathrate phase found by heats of formation calculations are in agreement with the accessed compositions. Chemical bonding analysis indicates two-center two-electron bonds for the covalent framework. XANES investigations suggest that the oxidation state of the Ni atoms in the Si-based type-I clathrates is close to that of elemental Ni. $Ba_{7.9}Ni_{1.6}Si_{44.4}$ and $Ba_{7.9}Ni_{1.7}Si_{44.3}$ are superconducting with onset T_c around 6.0 K and 5.5 K, respectively. The investigated annealed samples exhibit metallic-like behavior with moderate thermopower values at high temperatures. Thermal

conductivity values for all compositions are relatively low. A *ZT* value of 0.1 at 700 K was obtained for the x = 3.8 sample which may allow further enhancement via substitution of framework atoms with other elements.

ACKNOWLEDGMENT. The authors acknowledge Petra Scheppan, Monika Eckert, Renate Hempel-Weber and members of the Kompetenzgruppe Struktur for providing experimental support. C.C. acknowledges the financial support of the CNRS-MPG program.

Supporting Information. X-ray crystallographic files in cif format, some X-ray powder patterns, DSC results, some SEM pictures, tables for interatomic distances. This material is available free of charge via the Internet at http://pubs.acs.org.

REFERENCES

1. Kasper, J. S.; Hagenmuller, P.; Pouchard, M.; Cros, C., *Science* **1965,** *150*, 1713-1714.
2. Stefanoski, S.; Martin, J.; Nolas, G. S., *Journal of Physics-Condensed Matter* **2010,** *22*, 485404.
3. Yamanaka, S.; Horie, H.; Nakano, H.; Ishikawa, M., *Fullerene Science and Technology* **1995,** *3*, 21-28.

4. Kawaji, H.; Horie, H.; Yamanaka, S.; Ishikawa, M., *PHYSICAL REVIEW LETTERS* **1995,** *74*, 1427-1429.
5. Yamanaka, S., Enishi E.,Fukuoka, H. ,Yasukawa, M., *Inorganic Chemistry* **2000,** *39*, 56-58.
6. Fukuoka, H.; Kiyoto, J.; Yamanaka, S., *Journal of Solid State Chemistry* **2003,** *175*, 237-244.
7. Li, Y.; Zhang, R. H.; Liu, Y.; Chen, N.; Luo, Z. P.; Ma, X. Q.; Cao, G. H.; Feng, Z. S.; Hu, C. R.; Ross, J. H., *PHYSICAL REVIEW B* **2007,** *75*, -.
8. Li, Y.; Liu, Y.; Chen, N.; Cao, G. H.; Feng, Z. S.; Ross, J. H., *Physics Letters A* **2005,** *345*, 398-408.
9. Kamakura, N.; Nakano, T.; Ikemoto, Y.; Usuda, M.; Fukuoka, H.; Yamanaka, S.; Shin, S.; Kobayashi, K., *PHYSICAL REVIEW B* **2005,** *72*, -.
10. Kuznetsov V. L. , K. L. A., Kaliazin A. E., Rowe D. M., *JOURNAL OF APPLIED PHYSICS* **2000,** *87*, 7871-7875.
11. Bentien, A.; Nishibori, E.; Paschen, S.; Iversen, B. B., *PHYSICAL REVIEW B* **2005,** *71*, 144107.
12. Blake, N. P.; Bryan, D.; Latturner, S.; Mollnitz, L.; Stucky, G. D.; Metiu, H., *journal of Chemical Physics* **2001,** *114*, 10063-10074.
13. Rowe, D. M., *CRC handbook of thermoelectrics*. CRC Press: Boca Raton, Fl. ; London, 1995; p 701p.
14. Johnsen, S.; Bentien, A.; Madsen, G. K. H.; Nygren, M.; Iversen, B. B., *PHYSICAL REVIEW B* **2007,** *76*, 245126.
15. Bentien, A.; Johnsen, S.; Iversen, B. B., *PHYSICAL REVIEW B* **2006,** *73*, -.
16. Cordier G., W. P., *Journal of the Less Common Metals* **1991,** *169*, 291-302.
17. Candolfi, C.; Aydemir, U.; Ormeci, A.; Baitinger, M.; Oeschler, N.; Steglich, F.; Grin, Y., *PHYSICAL REVIEW B* **2011,** *83*, 205102.
18. Aydemir, U.; Candolfi, C.; Borrmann, H.; Baitinger, M.; Ormeci, A.; Carrillo-Cabrera, W.; Chubilleau, C.; Lenoir, B.; Dauscher, A.; Oeschler, N.; Steglich, F.; Grin, Y., *Dalton Transactions* **2010,** *39*, 1078-1088.
19. Akselrud, L. G.; Zavalii, P. Y.; Grin, Y.; Pecharsky, V. K.; Baumgartner, B.; Wölfel, E., *Materials Science Forum* **1993,** *335*, 133-136.
20. Newville, M., *Journal of Synchrotron Radiation* **2001,** *8*, 96-100.
21. Newville, M., *Journal of Synchrotron Radiation* **2001,** *8*, 322-324.
22. Ravel, B.; Newville, M., *Journal of Synchrotron Radiation* **2005,** *12*, 537-541.
23. Koepernik, K.; Eschrig, H., *PHYSICAL REVIEW B* **1999,** *59*, 1743-1757.
24. Perdew, J. P.; Wang, Y., *PHYSICAL REVIEW B* **1992,** *45*, 13244-13249.
25. Kittel, C., *Introduction to solid state physics*. 7th ed. ed.; Wiley: New York ; Chichester, 1996; p xi,673p.
26. Goebel, T.; Prots, Y.; Haarmann, F., *Zeitschrift Fur Kristallographie-New Crystal Structures* **2009,** *224*, 7-8.
27. Rabadanov, M. K.; Ataev, M. B., *Crystallography Reports* **2002,** *47*, 33-38.
28. Ackerbauer, S.; Krendelsberger, N.; Weitzer, F.; Hiebl, K.; Schuster, J. C., *Intermetallics* **2009,** *17*, 414-420.
29. Kohout, M., *International Journal of Quantum Chemistry* **2004,** *97*, 651-658.
30. Ormeci, A.; Rosner, H.; Wagner, F. R.; Kohout, M.; Grin, Y., *Journal of Physical Chemistry A* **2006,** *110*, 1100-1105.
31. Kohout, M. *Basin*, 4.3; Dresden, 2008.
32. Pani, A.; Palenzona, A., *Journal of Alloys and Compounds* **2008,** *454*, L1-L2.
33. Massalski, T. B.; Okamoto, H., *Binary alloy phase diagrams*. 2nd ed. ed.; ASM International: Materials Park, Ohio, 1990.
34. Nguyen, L. T. K.; Aydemir, U.; Baitinger, M.; Bauer, E.; Borrmann, H.; Burkhardt, U.; Custers, J.; Haghighirad, A.; Hofler, R.; Luther, K. D.; Ritter, F.; Assmus, W.; Grin, Y.; Paschen, S., *Dalton Transactions* **2010,** *39*, 1071-1077.
35. Pauling, L.; Marsh, R. E., *Proceedings of the National Academy of Sciences of the United States of America* **1952,** *38*, 112-118.
36. Davidson, D. W., *Canadian Journal of Chemistry* **1971,** *49*, 1224-1242.

37. von Schnering H. G.; Llanos, J.; Peters, K.; Baitinger, M.; Grin, Y.; Nesper, R., *Z. Kristallogr. NCS* **2011,** *226*, 9-10.
38. von Schnering, H. G.; Kroner, R.; Baitinger, M.; Peters, K.; Nesper, R.; Grin, Y., *Zeitschrift Fur Kristallographie-New Crystal Structures* **2000,** *215*, 205-206.
39. Melnychenko-Koblyuk, N.; Grytsiv, A.; Rogl, P.; Rotter, M.; Bauer, E.; Durand, G.; Kaldarar, H.; Lackner, R.; Michor, H.; Royanian, E.; Koza, M.; Giester, G., *PHYSICAL REVIEW B* **2007,** *76*, 144118.
40. Melnychenko-Koblyuk, N.; Grytsiv, A.; Rogl, P.; Rotter, M.; Lackner, R.; Bauer, E.; Fornasari, L.; Marabelli, F.; Giester, G., *PHYSICAL REVIEW B* **2007,** *76*, 195124.
41. Melnychenko-Koblyuk, N.; Grytsiv, A.; Fornasari, L.; Kaldarar, H.; Michor, H.; Rohrbacher, F.; Koza, M.; Royanian, E.; Bauer, E.; Rogl, P.; Rotter, M.; Schmid, H.; Marabelli, F.; Devishvili, A.; Doerr, M.; Giester, G., *Journal of Physics-Condensed Matter* **2007,** *19*, -.
42. Alleno, E.; Maillet, G.; Rouleau, O.; Leroy, E.; Godart, C.; Carrillo-Cabrera, W.; Simon, P.; Grin, Y., *Chemistry of Materials* **2009,** *21*, 1485-1493.
43. Bohme, B.; Aydemir, U.; Ormeci, A.; Schnelle, W.; Baitinger, M.; Grin, Y., *Science and Technology of Advanced Materials* **2007,** *8*, 410-415.
44. Wosylus, A.; Veremchuk, I.; Schnelle, W.; Baitinger, M.; Schwarz, U.; Grin, Y., *Chemistry-a European Journal* **2009,** *15*, 5901-5903.
45. Wopersnow, W.; Schubert, K., *Zeitschrift fuer Metallkunde* **1976,** *67*, 807-810.
46. Mansour, A. N.; Melendres, C. A., *Journal of Physical Chemistry A* **1998,** *102*, 65-81.
47. Crespin, M.; Levitz, P.; Gatineau, L., *Journal of the Chemical Society-Faraday Transactions Ii* **1983,** *79*, 1181-1194.
48. Bader, R. F. W., *Atoms in molecules : a quantum theory*. Clarendon Press: Oxford, 1990; p 438p.

Tables

Table 1 : Crystallographic data for $Ba_8Ni_{2.6}Si_{42.6}$, $Ba_8Ni_{3.2}Si_{43.0}$ and $Ba_8Ni_{3.7}Si_{41.8}$.

Composition	**$Ba_8Ni_{2.6}Si_{42.6}$**	**$Ba_8Ni_{3.2}Si_{43.0}$**	**$Ba_8Ni_{3.7}Si_{41.8}$**
Molar mass ($gmol^{-1}$)	2470.13	2477.25	2478.51

Crystal system; space group	Cubic; *Pm*-3*n* (no. 223)		
a (Å)	10.2982(1)	10.2922(1)	10.2906(1)
Number of reflections (PXRD)	66	64	61
Unit cell volume (Å^3)	1092.15(3)	1090.25(3)	1089.74(3)
Z; ρ_{calc}(g cm^{-3})	1; 3.7524(1)	1; 3.7764(1)	1; 3.7792(1)
Diffractometer	RIGAKU Spider		
λ (Å); monochromator	0.56087; multilayer-optics		
Crystal size (μm^3)	20 × 35 × 55	10 × 10 × 40	20 × 30 × 50
T (K)	295		
2θ range (°)	3.82 to 34.97	3.12 to 30.11	3.12 to 30.65
Indexes ranges	$-21 \le h \le 15$, $-16 \le k \le 12$, $-18 \le l \le 13$	$-3 \le h \le 15$, $-17 \le k \le 17$, $-17 \le l \le 18$	$-18 \le h \le 17$, $-18 \le k \le 15$, $-16 \le l \le 18$
μ (mm^{-1})	4.90	5.01	5.14
F(000) (e)	1128	1131	1132
Absorption correction	Multi-scan		
Reflections collected; unique	11916; 720 [Rint =0 .04]	6635; 503 [Rint =0 .04]	12195; 560 [Rint = 0.03]
Refined parameters	25	33	36
Refinement method	Full-matrix least-squares on *F*		
R(*F*); R(F^2) [$I > 4\sigma(I)$]	0.030; 0.021	0.023; 0.019	0.021; 0.022
Goodness-of-fit on *F*	1.92	1.71	1.46

Table 2: Atomic coordinates, displacement parameters (in Å^2) and site occupancies for $Ba_8Ni_{2.6}Si_{42.6}$ (top), $Ba_8Ni_{3.2}Si_{43.0}$(middle) and $Ba_8Ni_{3.7}Si_{41.8}$(bottom).

Atom	**Site**	***x***	***y***	***z***	***U*eq**	***Occ.***
Ba1	2*a*	0	0	0	0.00949(5)	1.0
Ba2	24*k*	0.2474(8)	0.5163(3)	0	0.0159(5)	0.25
Ni1/Si1	6*c*	1/4	0	1/2	0.0086(2)	0.433/0.55(1)

Si2	16*i*	0.18461(6)	*x*	*x*	0.00814(8)	1.0
Si31	24*k*	0	0.3087(2)	0.1164(2)	0.0089(3)	0.567(4)
Si32	24*k*	0	0.3148(2)	0.1279(2)	0.0097(4)	0.433
Atom	U_{11}	U_{22}	U_{33}	U_{12}	U_{13}	U_{23}
Ba1	0.00949(8)	U_{11}	U_{11}	0	0	0
Ba2	0.0122(5)	0.0145(6)	0.0211(10)	0.0040(6)	0	0
Ni1/Si1	0.0097(4)	0.0080(3)	U_{22}	0	0	0
Si2	0.0081(1)	U_{11}	U_{11}	-0.0008(1)	U_{12}	U_{12}
Si31	0.0095(5)	0.0068(5)	0.0106(5)	0	0	0.0012(4)
Si32	0.0066(6)	0.0128(7)	0.0098(7)	0	0	0.0020(6)

Atom	**Site**	***x***	***y***	***z***	***U*eq**	***Occ.***
Ba1	2*a*	0	0	0	0.00899(5)	1.0
Ba2	24*k*	0.24105(7)	0.51441(7)	0	0.0151(5)	0.25
Ni1/Si1	6*c*	1/4	0	1/2	0.0073(2)	0.533/0.404(7)
Si2	16*i*	0.18434(5)	*x*	*x*	0.00796(8)	1.0
Si31	24*k*	0	0.3067(2)	0.1122(2)	0.0063(4)	0.405(3)
Si32	24*k*	0	0.3151(2)	0.1281(2)	0.0074(3)	0.533
Si33	24*k*	0	0.3278(13)	0.1325(13)	0.009(2)*	0.063(3)
Atom	U_{11}	U_{22}	U_{33}	U_{12}	U_{13}	U_{23}
Ba1	0.00899(9)	U_{11}	U_{11}	0	0	0
Ba2	0.0019(2)	0.0188(10)	0.0315(10)	0.0027(5)	0	0
Ni1/Si1	0.0079(5)	0.0069(3)	U_{22}	0	0	0
Si2	0.0080(1)	U_{11}	U_{11}	-0.0006(2)	U_{12}	U_{12}
Si31	0.0082(7)	0.0069(7)	0.0037(7)	0	0	-0.0025(6)
Si32	0.0073(5)	0.0066(5)	0.0082(5)	0	0	-0.0001(4)

Atom	**Site**	***x***	***y***	***z***	***U*eq**	***Occ.***
Ba1	2*a*	0	0	0	0.01052(5)	1.0
Ba2	24*k*	0.24311(9)	0.51155(9)	0	0.0214(8)	0.25
Ni1/Si1	6*c*	1/4	0	1/2	0.0088(2)	0.617/0.231(8)
Si2	16*i*	0.18434(5)	*x*	*x*	0.00981(7)	1.0

Si31	24*k*	0	0.3072(3)	0.1094(3)	0.0076(6)	0.232(3)
Si32	24*k*	0	0.3122(1)	0.1231(1)	0.0099(3)	0.617
Si33	24*k*	0	0.3216(5)	0.1343(5)	0.0080(9)	0.152(4)
Atom	$\boldsymbol{U_{11}}$	$\boldsymbol{U_{22}}$	$\boldsymbol{U_{33}}$	$\boldsymbol{U_{12}}$	$\boldsymbol{U_{13}}$	$\boldsymbol{U_{23}}$
Ba1	0.01052(8)	U_{11}	U_{11}	0	0	0
Ba2	0.0085(2)	0.019(2)	0.037(2)	-0.0008(7)	0	0
Ni1/Si1	0.0090(3)	0.0082(2)	U_{22}	0	0	0
Si2	0.0098(1)	U_{11}	U_{11}	-0.0006(1)	U_{12}	U_{12}
Si31	0.0048(9)	0.0095(11)	0.0086(10)	0	0	-0.0006(8)
Si32	0.0119(4)	0.0089(4)	0.0089(4)	0	0	0.0016(3)
Si33	0.0040(2)	0.008(2)	0.012(2)	0	0	-0.0027(14)

$^{*}U_{iso}$

U_{eq} is defined as one third of the trace of the orthogonalized U_{ij} tensor, which is exp $(-2\pi^2\ [h^2a^{*2}U_{11} + ... + 2\ h\ k\ a^*\ b^*\ U_{12}])$

Table 3: The lattice parameter and composition of the samples obtained after annealing at 1000 ºC for 1 week.

Nominal composition	**Products**	**Composition (WDXS)**	***a* (Å)**

	PXRD & EDXS		
$Ba_8Ni_{0.2}Si_{45.8}$	C-I (< 10 %), $BaSi_2$ (> 40 %), α-Si (> 50 %)	$Ba_{8.0(3)}Ni_{2.5(1)}Si_{42.0(2)}$	10.2994(1)
$Ba_8Ni_{0.5}Si_{45.5}$	C-I (< 20 %), $BaSi_2$ (> 40 %), α-Si (> 40 %)	$Ba_{8.0(3)}Ni_{2.5(1)}Si_{42.3(3)}$	10.2997(1)
$Ba_8Ni_1Si_{45}$	C-I (> 40%), $BaSi_2$ (<30 %), α-Si (< 30 %)	$Ba_{8.00(3)}Ni_{2.43(2)}Si_{43.30(4)}$	10.3007(1)
$Ba_8Ni_2Si_{44}$	C-I (> 80%), $BaSi_2$ (<10 %), α-Si (< 10 %)	$Ba_{8.00(5)}Ni_{2.36(4)}Si_{43.94(6)}$	10.3011(2)
$Ba_8Ni_2Si_{44}$	C-I (> 80%), $BaSi_2$ (<10 %), α-Si (< 10 %)	$Ba_{8.00(3)}Ni_{2.44(2)}Si_{42.81(3)}$	10.3007(1)
$Ba_8Ni_{2.5}Si_{43.5}$	C-I (> 95%), $BaSi_2$ (<3 %), α-Si (< 2 %)	$Ba_{8.00(3)}Ni_{2.62(1)}Si_{42.57(3)}$	10.2982(1)
$Ba_8Ni_{2.5}Si_{43.5}$	C-I (> 95%), $BaSi_2$ (<3 %), α-Si (< 2 %)	$Ba_{8.00(2)}Ni_{2.64(2)}Si_{43.23(4)}$	10.2981(1)
$Ba_8Ni_{2.65}Si_{43.35}$	C-I (> 96%), $BaSi_2$ (<2 %), α-Si (< 2 %)	$Ba_{8.00(5)}Ni_{2.73(1)}Si_{42.89(5)}$	10.2958(1)
$Ba_8Ni_{2.75}Si_{43.25}$	C-I (> 98%), $BaSi_2$ (<1 %), α-Si (< 1 %)	$Ba_{8.00(2)}Ni_{2.81(2)}Si_{42.10(3)}$	10.2951(1)
$Ba_8Ni_{2.75}Si_{43.25}$	C-I (> 98%), $BaSi_2$ (<1 %), α-Si (< 1 %)	$Ba_{8.00(2)}Ni_{2.83(1)}Si_{42.61(1)}$	10.2947(1)
$Ba_8Ni_{2.85}Si_{43.15}$	C-I (> 98%), $BaSi_2$ (<1 %), α-Si (< 1 %)	$Ba_{8.00(1)}Ni_{2.93(1)}Si_{42.50(1)}$	10.2929(1)
$Ba_8Ni_3Si_{43}$	C-I (> 98%), $BaSi_2$ (<1 %), α-Si (< 1 %)	$Ba_{8.00(2)}Ni_{3.11(1)}Si_{42.26(2)}$	10.2923(1)
$Ba_8Ni_3Si_{43}$	C-I (> 98%), $BaSi_2$ (<1 %), α-Si (< 1 %)	$Ba_{8.00(2)}Ni_{3.17(1)}Si_{43.03(2)}$	10.2922(1)
$Ba_8Ni_{3.5}Si_{42.5}$	C-I (> 99%), α-Si (< 1 %)	$Ba_{8.00(7)}Ni_{3.42(3)}Si_{41.99(4)}$	10.2904(1)
$Ba_8Ni_{3.5}Si_{42.5}$	C-I (> 99 %), NiSi (< 1 %)	$Ba_{8.00(3)}Ni_{3.46(4)}Si_{41.56(7)}$	10.2897(1)
$Ba_8Ni_4Si_{42}$	C-I (> 98%), $BaSi_2$, NiSi, $NiSi_2$ (<2 %)	$Ba_{8.00(4)}Ni_{3.72(9)}Si_{41.83(5)}$	10.2906(1)
$Ba_8Ni_4Si_{42}$	C-I (> 98%), $BaSi_2$, NiSi, $NiSi_2$ (<2 %)	$Ba_{8.00(3)}Ni_{3.82(4)}Si_{41.33(6)}$	10.2896(1)
$Ba_8Ni_6Si_{40}$	C-I (> 90%), $BaSi_2$, NiSi, $NiSi_2$ (<10 %)	$Ba_{8.00(1)}Ni_{3.62(3)}Si_{41.16(3)}$	10.2907(1)
$Ba_8Ni_{10}Si_{36}$	C-I (> 70 %), $BaSi_2$, NiSi, $NiSi_2$ (<30 %)	$Ba_{8.00(1)}Ni_{3.71(3)}Si_{42.46(3)}$	-

Table 4: The lattice parameter and composition of the samples obtained after steel-quenching.

Nominal composition	Products (PXRD & EDXS)	Composition (PXRD & EDXS)	*a* (Å)

$Ba_8Ni_{0.2}Si_{45.8}$	C-I (< 5 %), $BaSi_2$ (> 40 %), α-Si (> 50 %)	$Ba_{7.9}Ni_{1.6}Si_{44.4}$	10.3088(1)
$Ba_8Ni_{0.5}Si_{45.5}$	C-I (< 10 %), $BaSi_2$ (> 40 %), α-Si (> 40 %)	$Ba_{7.9}Ni_{1.7}Si_{44.3}$	10.3078(1)
$Ba_8Ni_3Si_{43}$	C-I (> 60%), $BaSi_2$ (< 20 %), α-Si (< 20 %)	$Ba_8Ni_3Si_{45.6}$	10.2932(1)
$Ba_8Ni_{3.5}Si_{42.5}$	C-I (> 70%), $BaSi_2$ (< 15 %), α-Si (< 15 %)	$Ba_8Ni_3Si_{42.3}$	10.2927(1)
$Ba_8Ni_6Si_{40}$	C-I (> 80%), $BaSi_2$ (<15 %), NiSi(< 5 %)	$Ba_8Ni_{3.2}Si_{45.9}$	10.2935(1)

Table 5: ΔH_f (Eq. (1)) and ΔE (Eq. (2)) in units of meV atom^{-1} for $Ba_8Ni_x\square_ySi_{46-x-y}$. Negative values of ΔE indicate that the clathrate phase is more stable than the competing phases.

(x, y) for $Ba_8Ni_x\square_ySi_{46-x-y}$	**ΔH_f**	**ΔE**
(0, 0)	171.25	-1.76
(1, 0)	193.28	-2.23
(2, 0)	218.22	-5.58
(3, 0)	243.87	-9.67
(3, 1)	221.98	16.64
(4, 0)	256.96	-1.18
(4, 1)	231.33	29.35
(6, 0)	285.78	13.14

Figure Captions

Figure 1: Liquidus surface in the system $BaSi_2$ – NiSi – α-Si. The investigated compositions are numbered and discussed in the text in relation to the binary (ε) and ternary (τ) eutectics.

Figure 2: SEM images (BSE contrast) of the samples investigated for liquidus surface in the system $BaSi_2$ – NiSi – α-Si. The nominal compositions of the investigated samples are: (**a**) $BaNiSi_3$, (**b**) $Ba_8Ni_{0.5}Si_{45.5}$, (**c**) $Ba_{10}Ni_2Si_{88}$, (**d**) $Ba_8Ni_3Si_{43}$, (**e**) $Ba_8Ni_6Si_{40}$, (**f**, **f1**) $Ba_5Ni_{30}Si_{65}$ (**g**) $Ba_{25}Ni_5Si_{70}$, (**h**) $Ba_{20}Ni_{10}Si_{70}$, (**i**) $Ba_{12}Ni_{30}Si_{58}$, and (**j, j1**) $Ba_5Ni_{40}Si_{55}$. The regions shown in black belong to α−Si, in white to $BaSi_2$ and light grey to dark grey areas represent clathrate-I, NiSi or $NiSi_2$ phases. As the compositions containing heavy elements backscatter electrons more strongly, they appear brighter in the image. For details please see the text.

Figure 3: (**a**) Isothermal section of the system $BaSi_2$ – NiSi – α-Si at 1000 °C. Investigated compositions are numbered consecutively and explained in detail in the text. The part of the phase diagram which should be liquid at 1000 °C is only estimated and shown in green. (**b**) A focused region of isothermal section of the system $BaSi_2$ – NiSi – α-Si at 1000 °C. The homogeneity range of the clathrate phase is shown in grey area. The refined single crystal compositions are shown with squares.

Figure 4: Microstructure (SEM, BSE contrast) of samples investigated for isothermal section of the system $BaSi_2$ – NiSi – α-Si at 1000 °C. The nominal compositions of the investigated samples are (**a**) $Ba_8Ni_2Si_{44}$, (**b**) $Ba_{18}Ni_5Si_{77}$, (**c**) $Ba_{13}Ni_5Si_{82}$, and (**d**) $Ba_8Ni_{4.0}Si_{42.0}$. While the regions shown in black belong to α−Si and in white to $BaSi_2$, grey to dark grey areas represent clathrate-I, $NiSi_2$ or NiSi phases. As the compositions containing heavy elements backscatter electrons more strongly, they appear brighter in the image. For details please see the text.

Figure 5: Stability energy ΔE (Eq. 2) as a function of nominal Ni content. The inset displays the variation of heat of formation. The vacancy cases are not shown.

Figure 6: The crystal structure of the type-I clathrate. 20-atom and 24-atom polyhedra are shown in light and dark blue, respectively. Sites for Ba atoms (2*a*, 6*d*) and framework atoms (or vacancies; 6*c* (white), 16*i* (grey), 24*k* (red)) are illustrated.

Figure 7: Lattice parameter of samples for composition $Ba_{8-\delta}Ni_x\square_zSi_{46-x-y}$. (○) Lattice parameter of Ba_8Si_{46},[5] (◓) lattice parameter of samples obtained after fast cooling, (●) lattice parameter of annealed samples.

Figure 8: (**a**) Normalized Ni *K*-edge XANES spectra of clathrate samples for x = 2.5, 3.0, 3.5, 4.0 along with (**b**) Ni foil, NiSi, NiO and NiI_2 for comparison. Inset figure in (a) shows the normalized XAS of clathrate samples. Spectra are offset for clarity.

Figure 9: (**a**) k^2-weighted Ni *K*-edge EXAFS and (**b**) associated Fourier transform for clathrate samples.

Figure 10: Electron localizability indicator, ϒ , in $Ba_8Ni_4Si_{42}$: (**a**) ELI isosurface with ϒ = 1.33 around a six-ring whose 6*c* positions is occupied by Ni atoms, (**b**) ELI isosurface with ϒ = 1.33 around a six-ring whose 6*c* positions are occupied by one Ni and one Si atoms, (**c**) contour plot of the ELI distribution in the plane of a six ring revealing the structuring of the penultimate shells of the Ni (n = 3) and Ba2 (n = 5) atoms. Ni atoms are denoted by white, Si1 by yellow, Si2 by grey, Si3 by red, Ba1 by blue, and Ba2 by pink spheres.

Figure 11: (**a**) Electrical resistivity as a function of temperature of the x = 1.6 (○) and x = 1.7 (□) samples showing the superconducting transition which onsets at 6.0 and 5.5 K, respectively. (**b**) Evolution of the critical temperature, T_c, as a function of the Ni content, x. The T_c value of the Ba_8Si_{46} compound (x = 0) is taken from Yamanaka et al.[5] The solid line is a guide to the eye.

Figure 12: Temperature dependence of the electrical resistivity of the x = 2.6 (○), 2.8 (□), x = 3.1 (Δ), x = 3.5 (▼) and x = 3.8 (+) samples.

Figure 13: Temperature dependence of the thermopower of the x = 2.6 (○), 2.8 (□), x = 3.1 (Δ), x = 3.5 (▼) and x = 3.8 (+) samples.

Figure 14: Temperature dependence of (**a**) the total thermal conductivity, (**b**) the lattice and (**c**) electronic thermal conductivities of the x = 2.6 (○), 2.8 (□), x = 3.1 (Δ), x = 3.5 (▼) and x = 3.8 (+) samples.

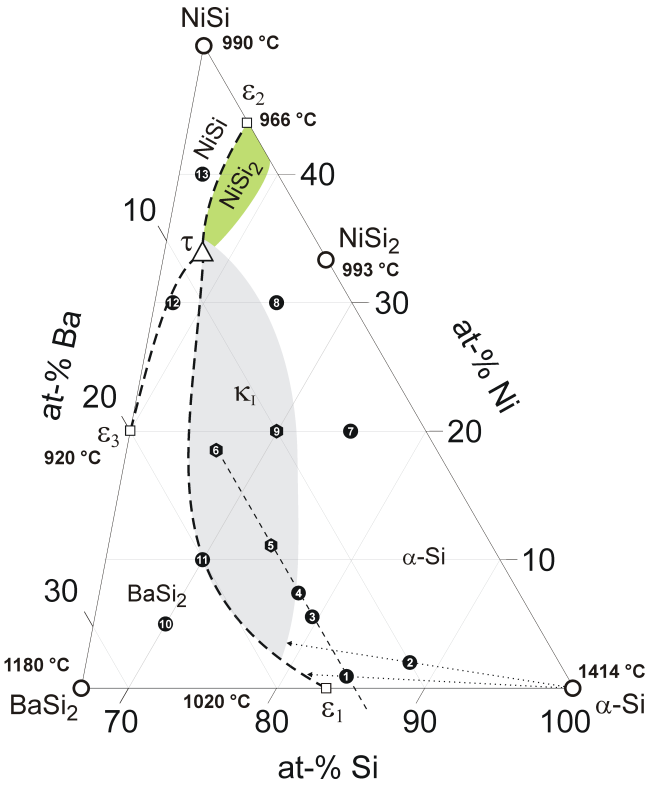
NiSi
990 °C
ε2
966 °C
NiSi
NiSi2
40
10
τ
NiSi2
993 °C
30
at-% Ni
at-% Ba
20
κI
ε3
920 °C
20
α-Si
10
30
BaSi2
1180 °C
1414 °C
BaSi2
1020 °C
ε1
70
80
90
100
α-Si
at-% Si

Fig. 1

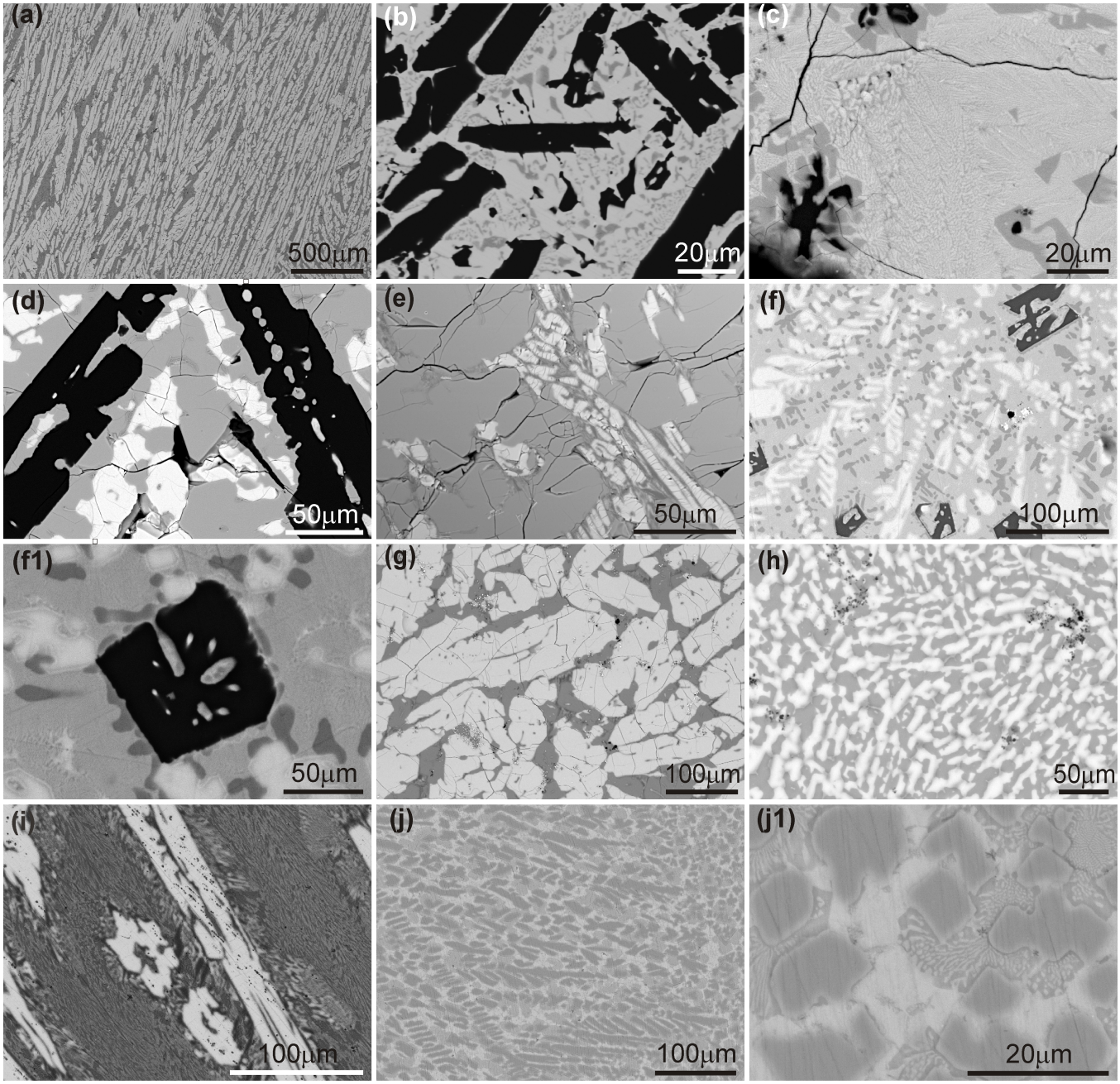
(a)
500μm
(b)
20μm
(c)
20μm
(d)
50μm
(e)
50μm
(f)
100μm
(f1)
50μm
(g)
100μm
(h)
50μm
(i)
100μm
(j)
100μm
(j1)
20μm

Fig. 2

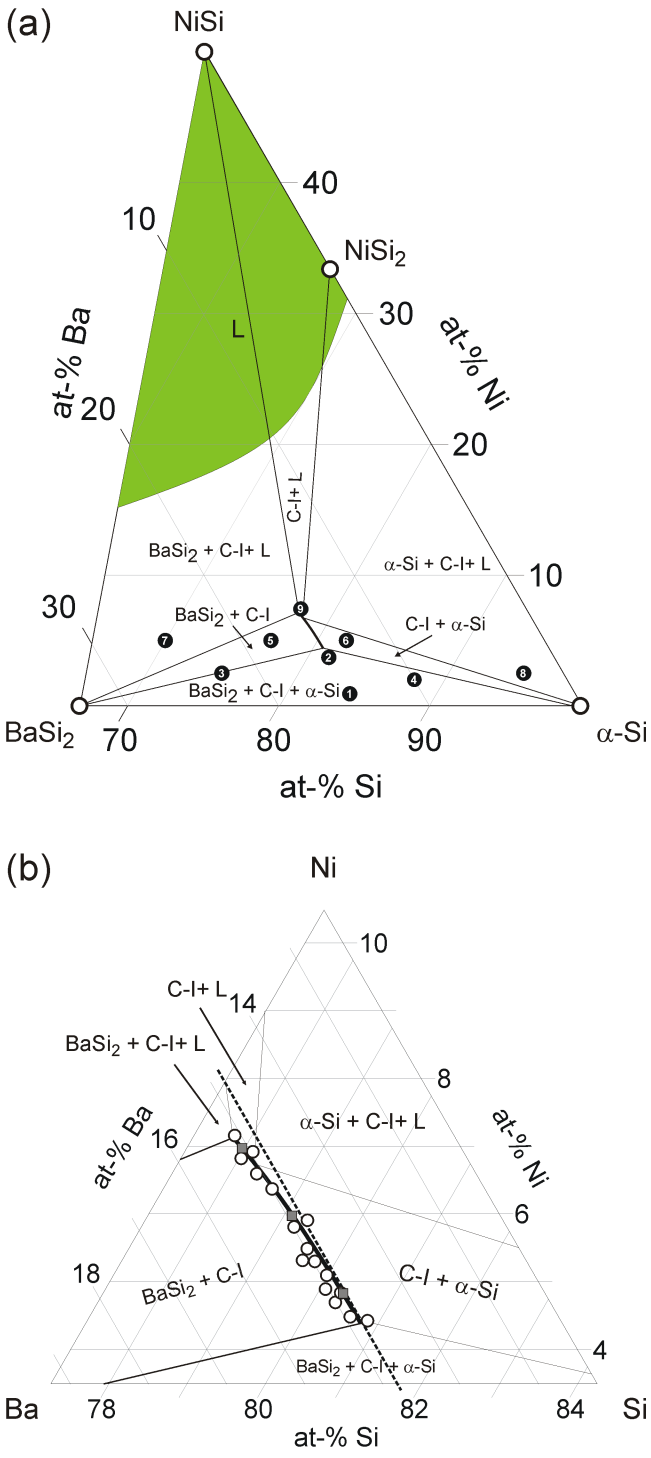
(a)
NiSi
NiSi2
L
C-I+ L
BaSi2 + C-I+ L
α-Si + C-I+ L
BaSi2 + C-I
C-I + α-Si
BaSi2 + C-I + α-Si
at-% Ba
at-% Ni
at-% Si
BaSi2
α-Si
10
20
30
40
70
80
90
(b)
Ni
C-I+ L
BaSi2 + C-I+ L
α-Si + C-I+ L
BaSi2 + C-I
C-I + α-Si
BaSi2 + C-I + α-Si
at-% Ba
at-% Ni
at-% Si
Ba
Si
8
14
16
18
6
4
78
80
82
84

Fig 3

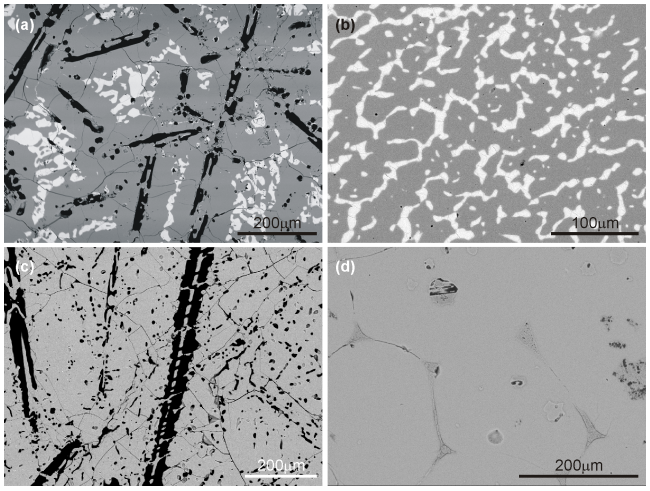

Fig. 4

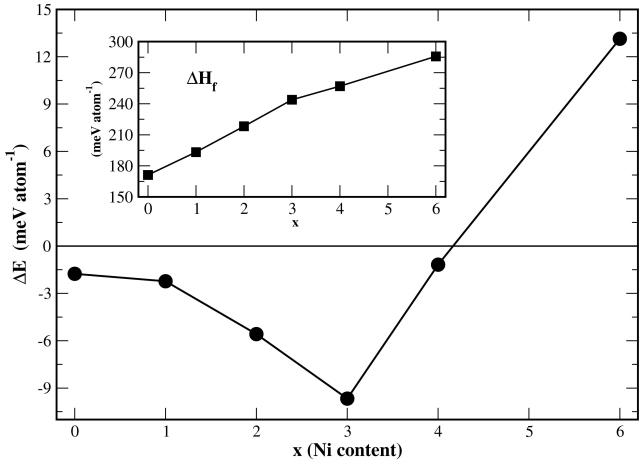

Fig. 5

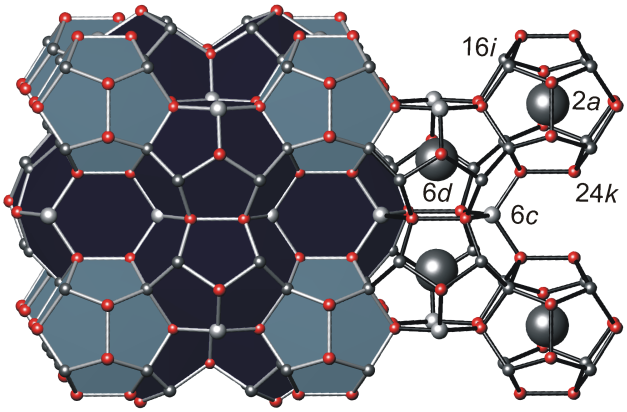

Fig. 6

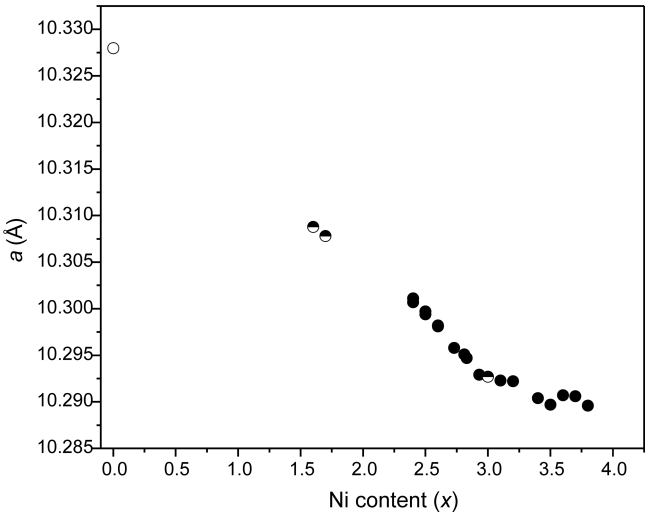
10.330
10.325
10.320
10.315
10.310
10.305
10.300
10.295
10.290
10.285
a (Å)
0.0
0.5
1.0
1.5
2.0
2.5
3.0
3.5
4.0
Ni content (x)

Fig. 7

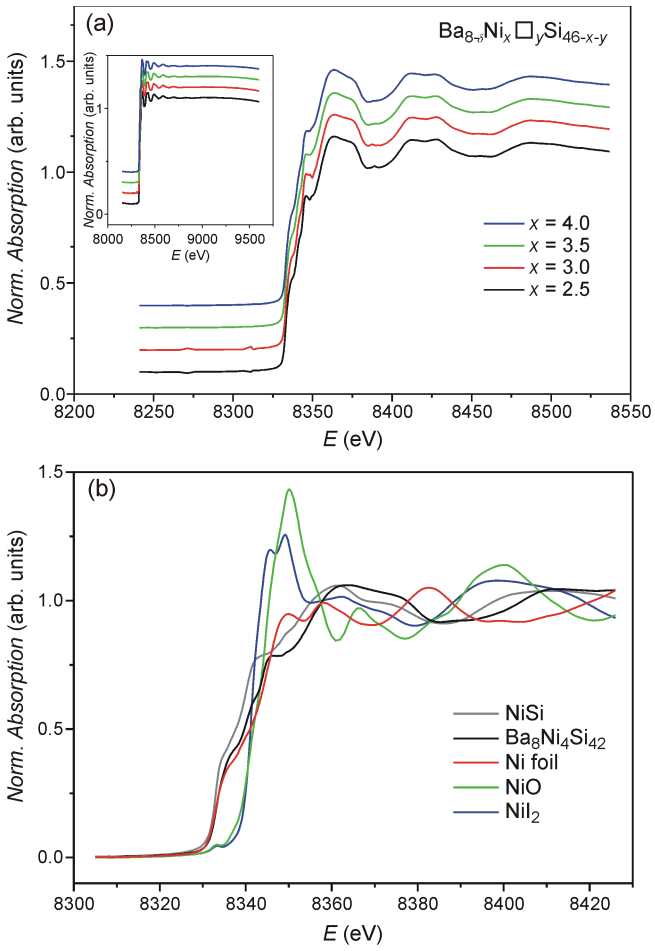
(a)
$Ba_{8-y}Ni_x\square_ySi_{46-x-y}$
Norm. Absorption (arb. units)
E (eV)
x = 4.0
x = 3.5
x = 3.0
x = 2.5
(b)
NiSi
$Ba_8Ni_4Si_{42}$
Ni foil
NiO
NiI_2

Fig. 8

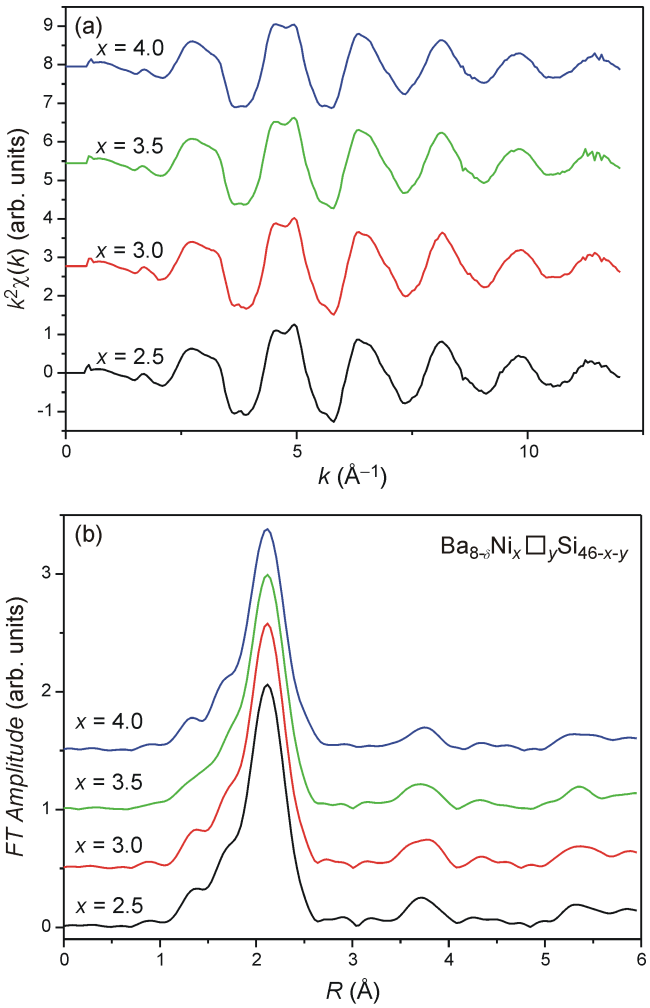
(a)
x = 4.0
x = 3.5
x = 3.0
x = 2.5
k²χ(k) (arb. units)
k (Å⁻¹)
(b)
Ba8-yNixOySi46-x-y
x = 4.0
x = 3.5
x = 3.0
x = 2.5
FT Amplitude (arb. units)
R (Å)

Fig. 9

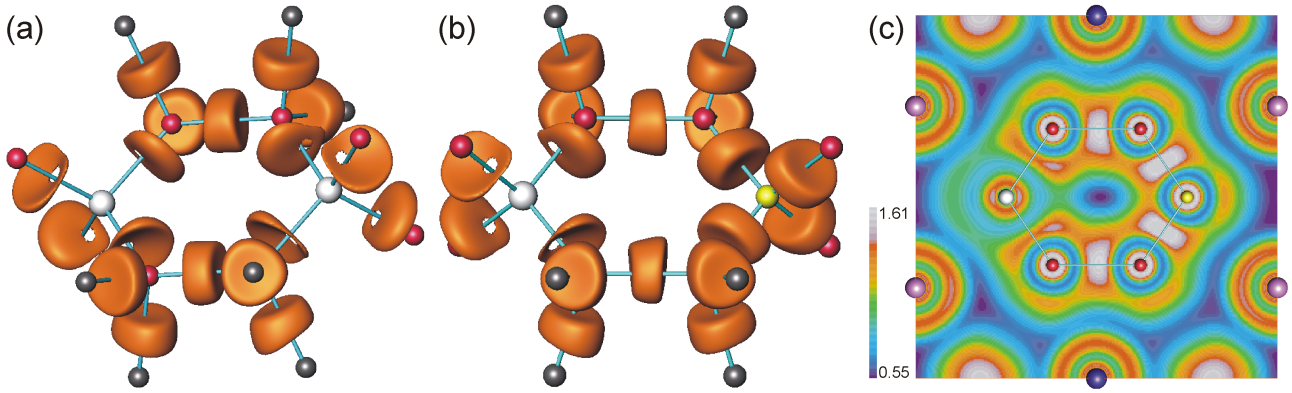

Fig. 10

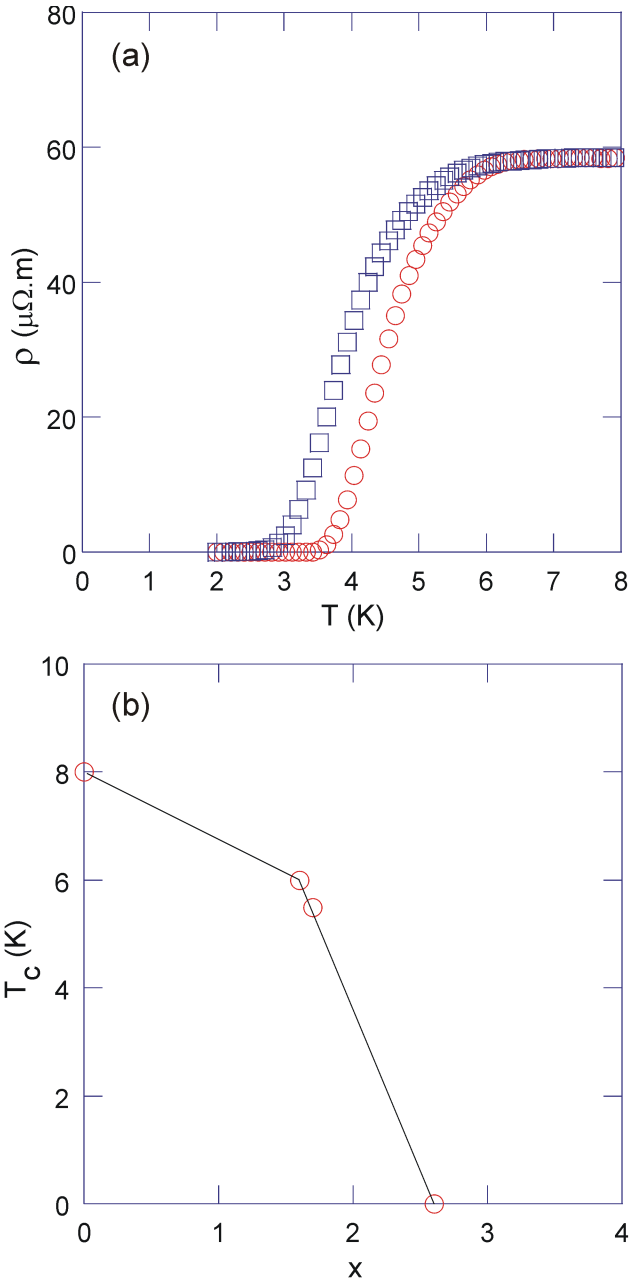

Fig. 11

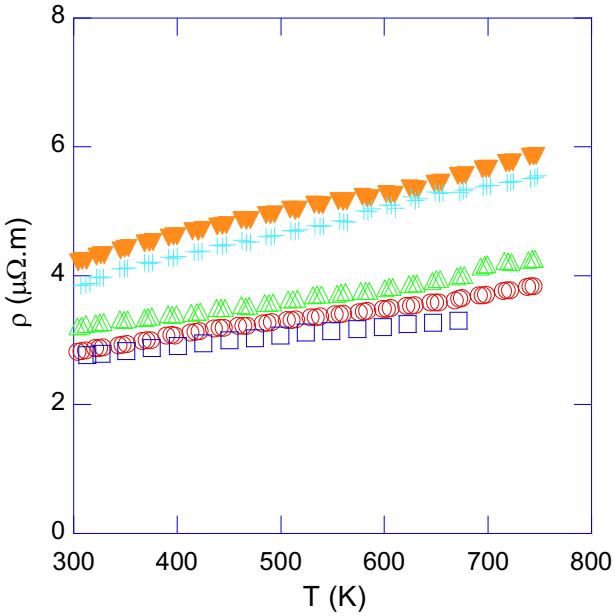
8
6
4
2
0
ρ (μΩ.m)
300
400
500
600
700
800
T (K)

Fig. 12

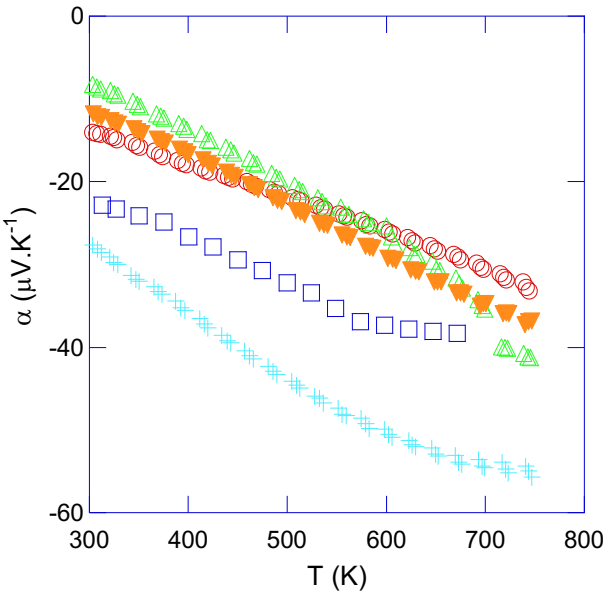
0
-20
-40
-60
α (μV.K-1)
300
400
500
600
700
800
T (K)

Fig. 13

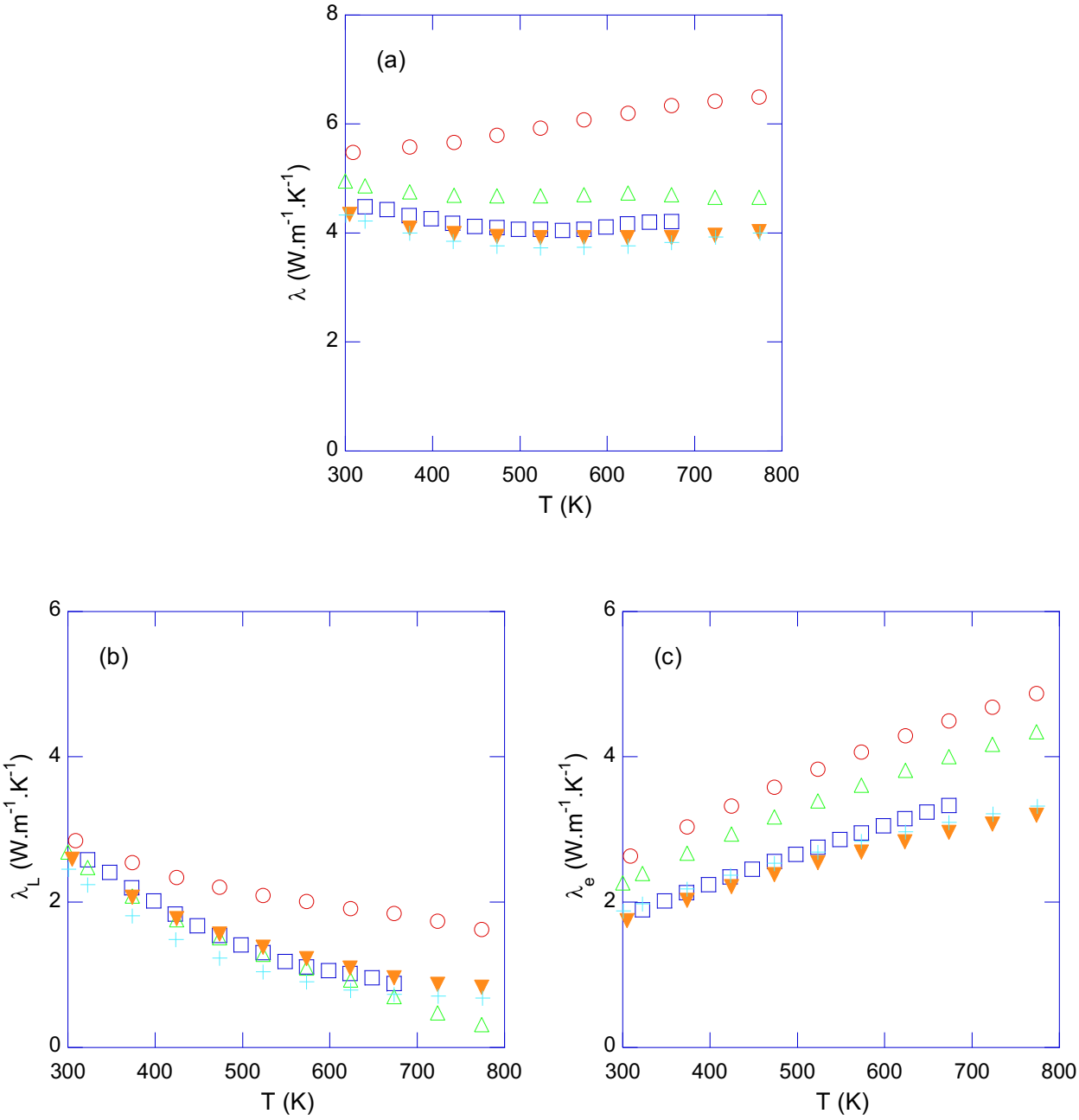

Fig. 14